

Numerical investigation of tandem-cylinder noise reduction using plasma-based flow control

Ahmed Eltaweel¹, Meng Wang^{1,†}, Dongjoo Kim², Flint O. Thomas¹ and Alexey V. Kozlov¹

¹Institute for Flow Physics and Control, Department of Aerospace and Mechanical Engineering, University of Notre Dame, Notre Dame, IN 46556, USA

²Department of Mechanical Engineering, Kumoh National Institute of Technology, Gumi, Gyeongbuk, Korea

(Received 24 November 2012; revised 9 June 2014; accepted 17 July 2014;
first published online 2 September 2014)

The noise of flow over tandem cylinders at $Re_D = 22\,000$ and its reduction using single dielectric barrier discharge (SDBD) plasma actuators are simulated numerically both to confirm and extend experimental results. The numerical approach is based on large-eddy simulation (LES) for the turbulent flow field, a semi-empirical plasma actuation model, and Lighthill's theory for acoustic calculation. Excellent agreement between LES and experimental results is obtained for both the baseline flow and flow with plasma control in terms of wake velocity profiles, turbulence intensity, and frequency spectra of pressure fluctuations on the downstream cylinder. The validated flow-field results allow an accurate acoustic analysis based on Lighthill's equation, which is solved using a boundary-element method. The effectiveness of plasma actuators for reducing noise is clearly demonstrated. In the baseline flow, the acoustic field is dominated by the interaction between the downstream cylinder and the upstream wake. Through suppression of vortex shedding from the upstream cylinder, the interaction noise is reduced drastically by the plasma flow control, and the vortex-shedding noise from the downstream cylinder becomes equally important. At a free-stream Mach number of 0.2, the peak sound pressure level is reduced by approximately 16 dB. This suggests the viability of plasma actuation for active aeroacoustic control of airframe noise.

Key words: aeroacoustics, flow control, turbulence simulation

1. Introduction

With the reduction in jet noise associated with the use of high-bypass-ratio engines on large- and medium-size civil transport aircraft, airframe noise has emerged as a primary noise source on approach and landing. A major component of airframe noise is the deployed landing gear configuration. The noise from the gear is broadband and originates due to complex, unsteady bluff body flow separation from gear components and the subsequent multiple interactions of unsteady wakes with downstream undercarriage elements.

[†] Email address for correspondence: m.wang@nd.edu

Tandem circular cylinders in a cross-flow configuration represent a generic flow geometry relevant to aircraft landing gear. Of particular interest is the nature of the interaction of the unsteady wake from the upstream cylinder with the downstream cylinder. Wake interactions of this type are expected to have a significant impact on the noise radiation associated with the aircraft undercarriage. In addition to the Reynolds number, the character of this interaction depends critically on the (centre-to-centre) cylinder separation, L , in relation to the diameter, D , of the cylinders. Due to the relevance of the tandem-cylinder configuration for heat exchangers and other industrial applications, it has been the subject of several previous investigations (Igarishi 1981, 1984; Ljungkrona, Norberg & Sundén 1991; Mittal, Kumar & Raghuvanshi 1997; Lin, Yang & Rockwell 2002; Jester & Kallinderis 2003). A comprehensive review of the flow around two circular cylinders of the same diameter in a tandem arrangement at subcritical Reynolds number is given by Zdravkovich (1985). According to Zdravkovich (1985), the flow exhibits many different vortex-shedding characteristics based on L/D . For $L/D > 3.8$, which is the case in the present study, constant vortex shedding occurs from both cylinders. The fluctuating pressure on circular cylinders in a tandem configuration was measured by Arie *et al.* (1983) in the upper subcritical regime. They found that the root-mean-square (r.m.s.) lift and drag was much larger on the downstream cylinder for L/D below 7 and became virtually identical on both cylinders for $L/D > 10$. The variation of Strouhal number with L/D for tandem-cylinder configurations at subcritical Reynolds numbers are reported by Xu & Zhou (2004).

Motivated by the landing gear noise issue, synergistic experimental and computational studies of tandem cylinders in cross-flow have been performed by the NASA Langley airframe noise group. Tandem-cylinder experiments performed at a Reynolds number of 1.66×10^5 for cases with $L/D = 1.44$ and 3.7 are reported by Jenkins *et al.* (2005, 2006). In these experiments the boundary layer on the upstream cylinder was tripped prior to separation. Measurements included mean and unsteady surface pressure, surface flow visualization as well as particle image velocimetry (PIV) measurement of the wake flow interaction with the downstream cylinder. Unsteady Reynolds-averaged Navier–Stokes (RANS) simulations of these experiments are reported by Khorrami *et al.* (2007). Mean flow quantities and vortex-shedding frequencies showed reasonable agreement with experiment for both values of cylinder spacing. More recently, the experimental database for the tandem-cylinder configuration was expanded as reported by Neuhaert *et al.* (2009). This study included measurements of fluctuating pressure on the downstream cylinder with high azimuthal resolution, high-resolution PIV measurement of the dynamics of the separating shear layer, as well as the influence of boundary layer trips on both upstream and downstream cylinders. In addition to measurements at $L/D = 1.44$ and 3.7, the case of $L/D = 3.04$ was also investigated which gave rise to a bistable, mode switching behaviour. Lockard *et al.* (2007) report tandem-cylinder noise predictions for the $L/D = 3.7$ case utilizing the CFL3D Navier–Stokes solver with a hybrid zonal turbulence model in conjunction with the Ffowcs Williams–Hawkings equation. The results indicate that pressure fluctuations on the upstream cylinder due to vortex shedding are small in relation to those on the downstream cylinder, which are associated with unsteady wake impingement. In this manner, the downstream cylinder dominates the noise radiation and produces a directivity pattern similar to that of an isolated cylinder. Corresponding numerical simulation results for the $L/D = 1.44$ case (subcritical spacing) are presented in Lockard *et al.* (2008).

As an aeroacoustics benchmark problem, the aforementioned NASA tandem-cylinder experiment with separation of $3.7D$, Reynolds number of 1.66×10^5 and Mach

number of 0.128 has been the subject of a number of recent numerical simulations. For example, Doolan (2009) used two-dimensional unsteady incompressible RANS equations solved with the OpenFOAM code to simulate the flow field, and Curle's formulation of the Lighthill theory (Curle 1955) in conjunction with a statistical model for spanwise and temporal source fluctuations to predict the acoustics. Although the simulation over-predicts the vortex-shedding frequency, the computed mean and unsteady flow results show general agreement with experimental data. The sound pressure level around the main shedding peak is predicted accurately, but the harmonic peaks and broadband content at high frequencies are over-predicted. Weinmann, Sandberg & Doolan (2010) evaluated several hybrid approaches combining RANS with large-eddy simulation (LES), which differ mainly in the way the RANS model is transformed into a subgrid-scale model, for the tandem-cylinder aeroacoustic prediction. They also used the OpenFOAM code for the flow-field simulation and Curle's theory for noise prediction. While the results are encouraging overall, deficiencies have been identified. Some approaches predict the flow field well but fail to capture accurately the higher harmonics and broadband noise levels at higher frequencies in the acoustic spectra. Others predict the higher harmonics in the acoustic spectra accurately but are deficient in predicting the hydrodynamic field. Brès *et al.* (2012) performed simulations of the NASA tandem-cylinder experiment using the lattice Boltzmann method in combination with the Ffowcs Williams–Hawkings equation. They included the full experimental span of $16D$ in the simulation and also considered the wind-tunnel installation effects caused by the open-jet nozzle and side plates. Overall agreement is obtained with experimental flow-field and acoustic data. The inclusion of side plates in the simulation is found to reduce the spanwise coherence, leading to more accurate predictions of the tonal-peak magnitude in the noise spectra.

Motivated by the need for landing gear noise reduction, Thomas, Kozlov & Corke (2008) and Kozlov & Thomas (2011a) conducted active flow control experiments on a single cylinder in cross-flow using single dielectric barrier discharge (SDBD) plasma actuators to reduce acoustic radiation by minimizing the unsteady flow separation and the associated large-scale wake vorticity. Two different actuator concepts were used: spanwise-oriented plasma actuators and plasma streamwise-vortex generators (PSVG). Both strategies significantly reduced the turbulence levels in the wake and consequently the noise levels. Spanwise and PSVG flow control showed nearly the same significant noise level reduction and a small contribution of the actuator-induced noise relative to the natural shedding noise was noticed.

Large-eddy simulation of the cylinder plasma flow control experiment reported in Thomas *et al.* (2008) was performed by Kim & Wang (2009). The effect of the plasma was modelled as a body force in the Navier–Stokes equations. Good agreement between the simulation and experiment was reported for both quasi-steady and pulsed plasma actuation. This study showed that large-scale vortex shedding is virtually eliminated by both steady and unsteady actuation, and the mean drag as well as drag and lift fluctuations are significantly reduced. The frequency of unsteady actuation was found to have a large effect on the control performance.

Kozlov & Thomas (2011b) extended their single-cylinder flow control work to the tandem-cylinder configuration as an idealization of the landing gear oleo–strut interaction. Both spanwise-oriented actuators and PSVG were applied to the upstream cylinder to reduce the pressure fluctuations on the downstream cylinder and consequently the noise emitted from both cylinders. They conducted experiments for Reynolds numbers ranging from 22 000 to 172 000 with centre-to-centre cylinder

separation of four diameters. All cases showed a dramatic reduction in pressure fluctuation levels on the downstream cylinder. However, no acoustic measurements were made due to limitations of the experimental facility.

The objective of the present work is to extend the experimental results of Kozlov & Thomas (2011b) to the acoustic field by numerical simulations and thereby demonstrate the efficacy of plasma flow control for noise reduction. A related objective is to clarify both the physics of noise production and the mechanism by which noise reduction occurs when plasma flow control is applied. To this end, LES in conjunction with a semi-empirical plasma actuation model is used to reproduce the experimental measurements of Kozlov & Thomas (2011b) for the flow field and surface-pressure fluctuations. To foster numerical accuracy, the lowest Reynolds number of $Re_D = 22\,000$ is considered. Once the flow field is validated by comparing velocity and surface-pressure statistics obtained from the numerical simulations and experiments, acoustic source terms are computed based on the LES velocity field. The acoustic field is then obtained by solving Lighthill's equation (Lighthill 1952) using a boundary-element method. Unlike the conventionally used Ffowcs Williams–Hawkings method, this approach allows the use of source data obtained from an incompressible flow solver while fully accounting for the acoustic interaction with both cylinders in a low-Mach-number flow. Furthermore, it facilitates the identification and analysis of important source regions. A detailed analysis is performed for the acoustic spectra, directivity, and source locations. The results clearly demonstrate the effectiveness of plasma-based flow control in noise reduction, and reveal the noise-reduction mechanisms. Furthermore, they exemplify how numerical and experimental techniques can complement each other synergistically to predict, understand and control flow-generated sound in practical configurations involving solid objects.

2. Overview of the experiment

The tandem-cylinder flow control experiment was performed in a low-turbulence, subsonic, in-draft wind tunnel located at the Hessert Laboratory for Aerospace Research at the University of Notre Dame. The wind tunnel has free-stream turbulence levels less than 0.1 % (and less than 0.06 % for frequencies above 10 Hz). Experiments were performed in a test section of 0.61 m² cross-section and 1.82 m in length. The free-stream velocity range was from 5.3 to 42 m s⁻¹ which corresponds to a Reynolds number range of 22 000–172 000. Only the $Re_D = 22\,000$ case which is used for validation of numerical simulations is presented in this paper. Further details regarding the experiment can be found in Kozlov & Thomas (2011b). Only essential aspects of the experiment are presented below.

The tandem-cylinder configuration used in the current study is represented by two circular cylinder models of nominally the same diameter that are mounted in the wind tunnel test section as shown schematically in figure 1. The upstream circular cylinder model is equipped with two spanwise-oriented SDBD plasma actuators as shown schematically in figure 2. It should be noted that the thickness of the surface electrodes is greatly exaggerated in the figure for the sole purpose of clearly illustrating their placement. These electrodes were made of 1.6 mil (0.041 mm) thick copper foil tape with acrylic adhesive. Furthermore, the electrodes were carefully mounted so as to achieve a hydraulically smooth surface. As such, the presence of the electrodes did not change the flow as verified by comparing baseline surface-pressure and wake measurements made with and without the electrodes on the cylinder surface.

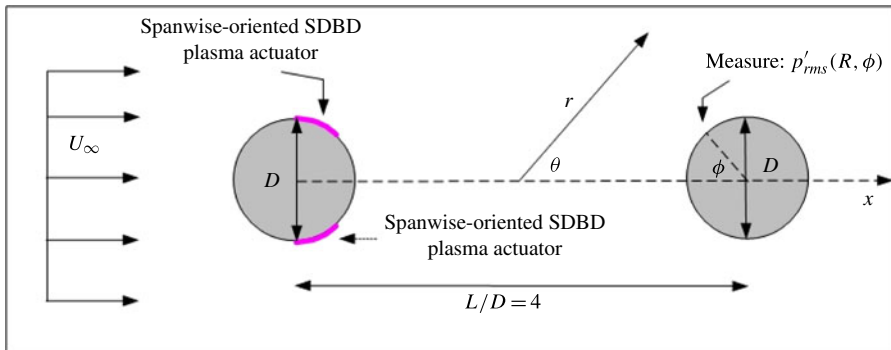


FIGURE 1. (Colour online) Schematic of the tandem-cylinder configuration.

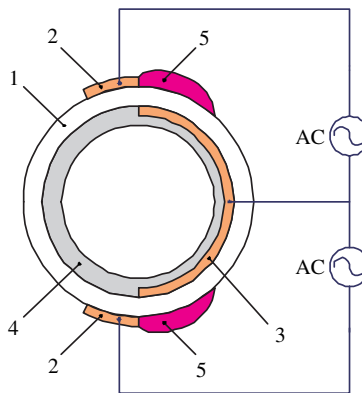


FIGURE 2. (Colour online) Schematic of the upstream-cylinder model with two spanwise-oriented SDBD plasma actuators. The surface electrode thickness is exaggerated.

In the experiments, transition occurred naturally and no effort was made to trip the cylinder boundary layers. Multiple trials of the experiment were performed and each measured quantity exhibited excellent repeatability. The upstream cylinder model is formed from a quartz glass cylinder (labelled (1) on figure 2) with an outer diameter $D = 65$ mm, wall thickness $d = 2.5$ mm, span of 533.4 mm and dielectric constant of 3.7. The cylinder wall serves as the dielectric barrier for the SDBD plasma. The ends of the cylinder terminate in endplates which elongates the model by 9.5 mm.

The covered electrodes were common for both plasma actuators due to space limitations. As indicated in figure 2, the outer, exposed electrode (2) was mounted on the surface of the cylinder with its plasma-generating edges located at $\pm 90^\circ$ with respect to the approach flow direction. This choice for the electrode positioning was based upon the idea that the best location for the plasma actuators is near the flow separation point. The covered electrode (3) was mounted on the inner surface of the cylinder. Both inner and outer electrodes extended 0.457 m in the spanwise direction which is equivalent to approximately 85% of the total span of the model.

For both actuators, eight layers of 5 mil (0.127 mm) Kapton tape (4) covered the inner electrodes and served to prevent inner discharge. The inner and outer electrodes for the spanwise actuator had a small overlap, which gave rise to a large local electric

field gradient. Plasma (5) formed near the edge of the exposed electrode and extended a distance along the cylinder dielectric surface as depicted in figure 2. As indicated in the figure, the actuators were connected to a high voltage a.c. source.

In this study, the spanwise actuator used a positive sawtooth waveform a.c. voltage of 55 kV peak-to-peak at 1 kHz. The sawtooth waveform has been shown to be optimum in terms of giving rise to the largest body force (Thomas *et al.* 2009). Frequencies for SDBD plasma actuation typically range from 1 to 10 kHz. The relatively low frequency used in this experiment was based on the observation reported in Thomas *et al.* (2009) that maintenance of a volumetric plasma discharge at high voltage is associated with operation of the actuators at lower a.c. frequencies.

The downstream cylinder was not instrumented with plasma actuators. The line of separation between the centres of the two cylinders was parallel to the oncoming flow. The distance between the axes of the two cylinders was 260 mm ($L/D = 4$). This separation distance was chosen to purposely avoid the bistable behaviour reported in previous studies for smaller L/D (Zdravkovich 1985). The length of the second cylinder was 550 mm. The tunnel blockage due to the tandem-cylinder model and support was less than 9%. Due to the relatively low blockage and since a focus of the experiment was on comparing the natural and plasma-actuated tandem-cylinder flow fields, no blockage corrections were applied to the experimental results presented in the paper. In order to measure the r.m.s. unsteady surface-pressure distribution as a function of angular position ϕ with a single probe, one end of the cylinder was attached to the shaft of a stepper motor installed on the test section wall. The motor had 48 steps per revolution resulting in the rotation of the downstream cylinder model with a $\Delta\phi = 7.5^\circ$ increment. The other end of the cylinder was connected to the wall of the test section with a bearing. The unsteady surface pressure was measured with a flush-mounted, high-frequency response, miniature differential pressure sensor. This transducer had a diameter of 2.34 mm and is positioned at the mid-span on the downstream cylinder. The pressure was measured relative to the static pressure in the uniform flow in front of the model. Measurements of both the mean and unsteady r.m.s. pressure distributions on the downstream cylinder were performed for both the baseline and plasma control cases. The relative uncertainty for the mean and r.m.s. pressure coefficient measurements is $\pm 3.0\%$.

In addition to the surface-pressure measurements, non-intrusive, two-component velocity measurements were conducted midway between the two cylinders using a laser Doppler anemometry (LDA) system. The fibre-optic LDA system was operated in 180° backscatter mode. The optical configuration produced a probe volume of dimension 0.2 mm in both the streamwise and cross-stream directions. This defines the effective spatial resolution for the LDA measurements. At 95% confidence, the mean velocity measurements have a $\pm 3.3\%$ relative uncertainty. Turbulence intensity measurements have a relative uncertainty of $\pm 3.5\%$.

3. Numerical approach

3.1. Flow simulation

Large-eddy simulations of the tandem-cylinder flow and its plasma control are carried out using a finite-volume, unstructured-mesh, incompressible LES code developed at Stanford University (Mahesh, Contantinescu & Moin 1998) with the addition of a plasma actuation model. This computational approach was previously used by Kim & Wang (2009) to simulate the plasma-based control of flow over a single cylinder. The cell-based code is energy-conservative, low-dissipative and second-order accurate

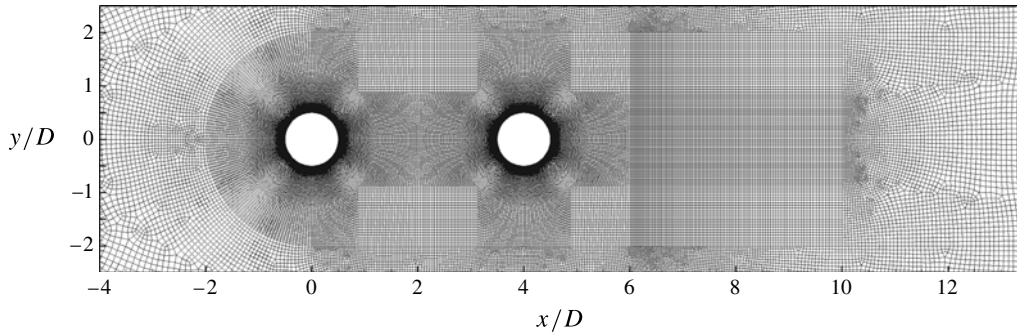


FIGURE 3. A two-dimensional cut of the coarse mesh near the tandem cylinders.

in space and time. The time marching scheme is fully implicit and based on the fractional step method. The pressure Poisson solver is of algebraic multi-grid type. The dynamic Smagorinsky model is used to model the effect of subgrid-scale stresses.

The computational domain extends in the streamwise direction from $-15D$ to $25D$. In the transverse direction, the computational domain conforms with the wind-tunnel walls located at $\pm 5D$, which ensures that the blockage effect in the experiment is appropriately accounted for. The domain is πD long in the spanwise direction. The centre of the first cylinder is defined as the origin of the coordinate system, and the centre of the second cylinder is $4D$ downstream from the centre of the first cylinder. The velocity at the inlet is uniform and equal to the free-stream velocity U_∞ . At the exit, a convective boundary condition is used to allow wake vortical structures to leave the computational domain smoothly. A periodic boundary condition is used in the spanwise direction. For the upper and lower boundaries, a stress-free boundary condition, which sets the wall-normal velocity and the wall-normal derivative of tangential velocities to zero, is employed. This condition allows the tunnel-wall blockage effect to be accounted for without resolving the wall boundary layers.

Two computational meshes were generated for a grid-convergence assessment. Both meshes are designed similarly to capture the boundary layers and separated shear layers from both cylinders. Structured quadrilateral cells are used around each cylinder, between the two cylinders, and in the wake of the second cylinder extending $6D$ downstream. The fine mesh, which is used to generate all the results in this paper, has 1.73×10^7 cells with 96 cells uniformly distributed in the spanwise direction and 400 cells in the circumferential direction for each cylinder. The smallest normal spacing is $6 \times 10^{-4}D$ over the first cylinder and $8 \times 10^{-4}D$ for the second cylinder with a stretching ratio of 1.05 in the normal direction. In contrast, the coarse mesh consists of only 4×10^6 cells with 48 cells uniformly distributed in the spanwise direction and 200 cells in the cylinder circumferential direction. The characteristics of the structured zones around the two cylinders are the same for both meshes. Figure 3 shows a close-up view of the coarse mesh around the tandem cylinders. The two grids yielded similar solutions as will be shown in § 4.

The effect of SDBD plasma actuation on the flow is modelled as a body force incorporated into the momentum equations in the LES code. The actuation is modelled as quasi-steady, given the short a.c. period relative to the important flow time scales. For example the a.c. actuation frequency is approximately 60 times the vortex-shedding frequency. In the present study, the simple model of Suzen *et al.* (2005) is used to estimate the body-force field generated by the spanwise plasma

actuators on the first cylinder as in the experimental set-up. It should be noted that plasma modelling is not a focus of this work. Certainly there are more complex plasma models available as described in the review by Corke, Enloe & Wilkinson (2010). However, with calibration, the semi-empirical model of Suzen *et al.* (2005) will be shown capable of providing velocity statistics and surface-pressure spectra in excellent agreement with experimental data, which allows acoustic source functions to be computed accurately from the simulated flow field. In this model, the electric potential is split into two parts: $\Phi = \phi + \varphi$, where φ is the internal potential field and ϕ is the external potential field due to the applied voltage. This, together with the Boltzmann assumption, leads to $\nabla \cdot (\epsilon_r \nabla \phi) = 0$ and $\nabla \cdot (\epsilon_r \nabla \rho_c) = -\rho_c / \lambda_D^2$, where ρ_c is the net charge density, λ_D is the Debye length, and ϵ_r is the relative permittivity. Once these two equations are solved numerically, the body force is calculated from $\mathbf{F} = -\rho_c \nabla \phi$. There are two model parameters which are tuned to generate the best fit with the experimental mean velocity profiles in the wake of the first cylinder. They are the Debye length, $\lambda_D = 1.7$ mm, and the maximum net charge density on the actuator surface, $\rho_{c,max} = 0.0025$ C m⁻³. These values were determined iteratively by first using coarse-mesh simulations to narrow down the parameter range followed by fine-mesh simulations for final adjustment. It is found that the overall momentum added is mainly affected by the maximum charge density, whereas the size of the effective plasma region is more sensitive to the Debye length. The computed flow statistics are more sensitive to the maximum charge density than the Debye length, but overall the sensitivities are not very high near the optimal values of model parameters. For example, with a $\pm 20\%$ change in $\rho_{c,max}$ the centreline mean velocity and turbulence intensity at $x/D = 2$ (half-way between the two cylinders) are changed by no more than 10% and 7%, respectively, whereas with a $\pm 20\%$ change in λ_D the mean velocity and turbulence intensity at the same position are changed by at most 6% and 3%, respectively.

3.2. Acoustic calculation

For sound calculations, as the flow is at low Mach number, the hybrid approach based on LES and Lighthill's theory is efficient and accurate (Wang, Freund & Lele 2006). The Lighthill equation in the form of a convected wave equation in the frequency domain can be written as

$$\left[\left(ik + M_i \frac{\partial}{\partial x_i} \right)^2 - \frac{\partial^2}{\partial x_j \partial x_j} \right] \tilde{p} = \frac{\partial^2 \tilde{T}_{ij}}{\partial x_i \partial x_j}, \quad (3.1)$$

where p is the pressure perturbation which is equal to the acoustic pressure p_a outside the nonlinear flow region, $M_i = U_i / c_\infty$ is the convection Mach number with $U_i = U_\infty \delta_{i1}$ and c_∞ being the sound speed in the free stream, $k = \omega / c_\infty$ is the acoustic wavenumber (ω is the angular frequency), and the tilde indicates a temporal Fourier transform. Since the flow is at low Mach number and moderately high Reynolds number without strong temperature inhomogeneities, the entropy and viscous contributions to the Lighthill stress are negligible, and the Lighthill stress tensor $T_{ij} \approx \rho_\infty (u_i - U_i)(u_j - U_j)$ where ρ_∞ is the free-stream density. To solve the Lighthill equation using a boundary-element method, the approach of Khalighi *et al.* (2010) is followed. Equation (3.1) along with a hard-wall boundary condition on the solid surfaces are recast into a boundary-integral equation,

$$\alpha \left(\tilde{p} + \frac{\tilde{T}_{ii}}{d} \right)_{\mathbf{x},k} = \int_{\partial\Omega \setminus \{\mathbf{x}\}} \tilde{p}(\mathbf{y}, k) n_i(\mathbf{y}) \frac{\partial G(\mathbf{x}|\mathbf{y}; k)}{\partial y_i} d^2\mathbf{y} + \int_{\Omega \setminus \{\mathbf{x}\}} \tilde{T}_{ij}(\mathbf{y}, k) \frac{\partial^2 G(\mathbf{x}|\mathbf{y}; k)}{\partial y_i \partial y_j} d^3\mathbf{y}, \quad (3.2)$$

where $G(\mathbf{x}|\mathbf{y}, k)$ is the free-space Green's function, \mathbf{x} and \mathbf{y} denote the observer and acoustic source locations, respectively, $n_i(\mathbf{y})$ is the solid surface unit normal into the fluid, $\partial\Omega$ is the solid surface, Ω is the source domain, α is equal to $1/2$ when $\mathbf{x} \in \partial\Omega$ and 1 when $\mathbf{x} \in \Omega$, and d is the dimension of the problem. The volume integral in (3.2) represents the direct radiation of sound by aerodynamic sources as equivalent quadrupoles in free space, whereas the surface integral represents the scattering effect of solid surfaces, which promotes efficient conversion of flow energy to acoustic energy. For a far-field observer in the mid-span plane ($z=0$), the source field in the computational domain is periodic and acoustically compact in the spanwise direction. This allows a spanwise Fourier transform of (3.1) and retaining only the zeroth spanwise Fourier mode, resulting in an equivalent two-dimensional problem with spanwise-averaged Lighthill source terms. Equation (3.2) is thus solved in two dimensions using Lighthill stress terms obtained from LES. The corresponding two-dimensional Green's function is

$$G(\mathbf{x}|\mathbf{y}, k) = -\beta \exp(iMk\beta^2(x_1 - y_1)) \frac{i}{4} H_0^{(2)}(\beta k|\mathbf{x}' - \mathbf{y}'|), \quad (3.3)$$

where $\beta = 1/\sqrt{1-M^2}$, x_1 and y_1 are the streamwise coordinates of the observer and source locations, respectively, $H_0^{(2)}$ is the Hankel function of the second kind, $\mathbf{x}' = (\beta x_1, x_2, x_3)$, and $\mathbf{y}' = (\beta y_1, y_2, y_3)$. The acoustic pressure solution is then converted to a three-dimensional solution in the mid-span far field using (Oberai, Roknaldin & Hughes 2002)

$$\tilde{p}_a^{3D}(r, \theta, z=0) \approx \tilde{p}_a^{2D}(r, \theta, z=0) \frac{1+i}{2} \sqrt{\frac{k}{\pi r}}, \quad (3.4)$$

where r and θ are the polar coordinates of the observer. Once the acoustic power spectrum is obtained from the source region in the computational domain of spanwise size L_z , the sound spectrum from the entire span S in the experiment is equal to S/L_z times the former spectrum, assuming that the source field is decorrelated within the spanwise computational domain size L_z .

3.3. Validation

The computational approaches for both flow and acoustics have been validated extensively. The flow solutions for tandem cylinders with and without control are compared with experimental measurements in §4. Since no acoustic data are available from the experiment, and since the main objective of the present work is to extend the experimental results to the acoustic field, an accurate acoustic solution method is critical. Evidence of accurate predictions by the solution method described in §3.2, and hence its predictive capability for the tandem-cylinder sound, is presented in the appendix by considering two closely related aeroacoustic problems of comparable complexity, for which acoustic data from either direct computation or experimental measurements are available in the literature. The first one is the flow over a single circular cylinder at $Re_D = 10\,000$ and free-stream Mach number of 0.2 . The acoustic prediction was shown to agree well with the sound computed by directly solving the compressible Navier–Stokes equations (Khalighi *et al.* 2010). In the second case, the sound of flow over a rod–airfoil configuration was computed, and the results showed excellent agreement with the experimental measurements of Jacob *et al.* (2005). Additionally, the same method was used recently to compute the sound from small steps and gaps in turbulent boundary layers (Hao, Eltaweel & Wang 2013a; Hao *et al.* 2013b). The results were consistent with those obtained using an approximate tailored Green's function for acoustically compact step and gap sizes.

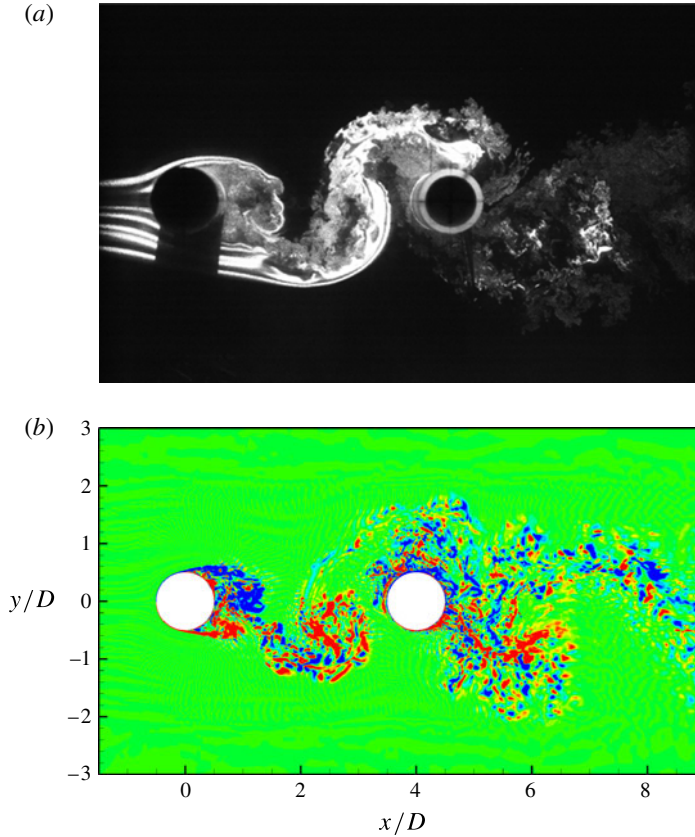


FIGURE 4. (Colour online) Instantaneous flow field without flow control. (a) Snapshot of the flow field from flow visualization; (b) spanwise vorticity $\omega_z D/U_\infty$ from LES (contour levels from -5 to 5 with increment 1).

4. Flow-field results

Instantaneous flow-field realizations from LES and experimental visualization (Kozlov & Thomas 2011b) of flow over tandem cylinders are shown in figures 4 and 5 for baseline and plasma controlled cases, respectively. The LES result, obtained on the fine mesh, depicts the spanwise vorticity field. For the baseline case (figure 4), both numerical and experimental results show qualitatively similar flow features in terms of shear-layer separation points, large-scale shedding structures behind the first cylinder, as well as interaction of wake structures with the downstream cylinder. Because of the strong wake impingement, the second cylinder does not produce discernible vortex shedding of its own. The coherent vortex shedding from the upstream cylinder and the impingement of the shed vortices on the downstream cylinder are sources of large-amplitude pressure fluctuations.

For the controlled case (figure 5), the effect of plasma-induced flow control is clearly demonstrated in both experimental and numerical results. The separation from the first cylinder is delayed, the wake becomes much narrower, and vortex shedding is largely suppressed. On the other hand, the second cylinder now produces its own coherent vortex shedding.

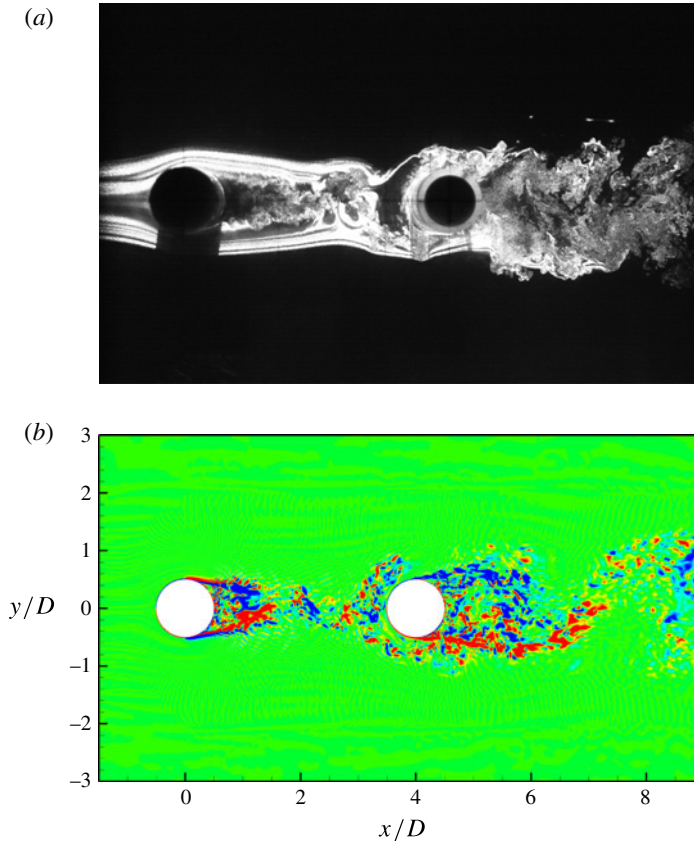


FIGURE 5. (Colour online) Instantaneous flow field with plasma flow control. (a) Snapshot of the flow field from flow visualization; (b) spanwise vorticity $\omega_z D/U_\infty$ from LES (contour levels from -5 to 5 with increment 1).

Figure 6 shows a comparison between numerical and experimental results for the baseline case. Shown are the mean streamwise velocity and r.m.s. of streamwise and cross-stream velocity fluctuations at $x = 2D$, which is midway between the two cylinders, for the baseline case. The numerical results are calculated by taking averages in the spanwise direction and over a time period of $120D/U_\infty$. Solutions from both coarse-mesh and fine-mesh simulations are shown. It can be noted that the numerical solutions are in good agreement with experimental results, and the fine-mesh and coarse-mesh results are in close agreement. The peak differences between the fine-mesh and coarse-mesh solutions are within 0.7% for the mean streamwise velocity, 4.2% for the r.m.s. of the streamwise velocity fluctuations, and 4.9% for the r.m.s. of the cross-stream velocity fluctuations, which demonstrates that the numerical solutions are grid insensitive.

A comparison of velocity statistics at $x = 2D$ between baseline and controlled cases from both LES and the experiment are shown in figure 7. The streamwise mean velocity and r.m.s. of velocity fluctuations are both in good agreement with experimental measurements for the controlled case as well. Although the plasma model was calibrated to match only the experimental mean streamwise velocity, the turbulence statistics are also well predicted. Plasma flow control is seen to drastically

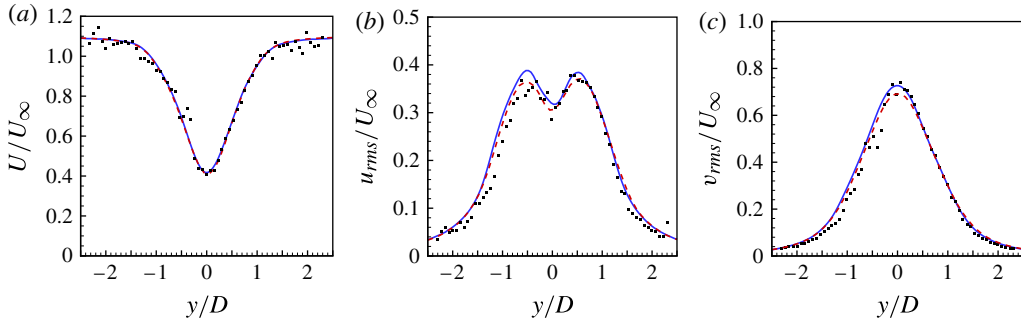


FIGURE 6. (Colour online) Velocity statistics at $x=2D$ for the baseline case. (a) Mean streamwise velocity; (b) r.m.s. of streamwise velocity fluctuations; (c) r.m.s. of cross-stream velocity fluctuations. ----, Coarse-mesh LES; —, fine-mesh LES; ■, experiment.

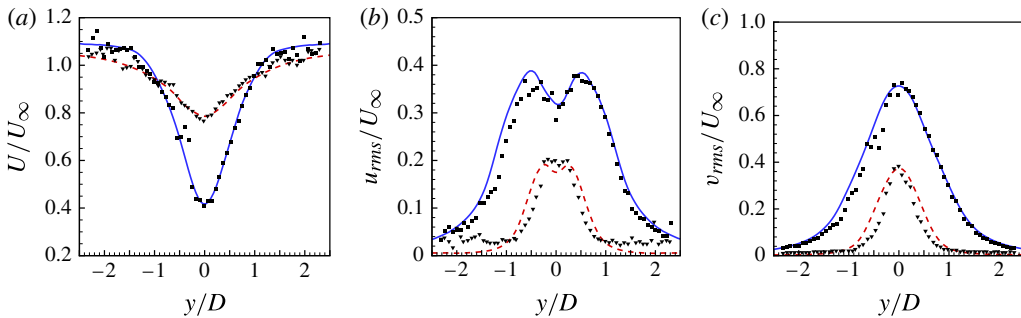


FIGURE 7. (Colour online) Comparison of velocity statistics at $x=2D$ for the baseline and controlled cases. (a) Mean streamwise velocity; (b) r.m.s. of streamwise velocity fluctuations; (c) r.m.s. of cross-stream velocity fluctuations. —, LES for baseline case; ■, experiment for baseline case; ----, LES for controlled case; ▼, experiment for controlled case.

reduce the wake mean velocity deficit and turbulence fluctuation levels. The wake profiles in the controlled case are much narrower than those in the baseline case, consistent with the observation made in figures 4 and 5.

Figure 8 shows the mean pressure coefficient and the coefficient of the r.m.s. of pressure fluctuations over the surface of the downstream cylinder, obtained from LES and the experiment for baseline and controlled cases. In the baseline case, LES predicts a lower front stagnation pressure and higher pressure fluctuation levels compared to the experiment, but experimental errors, noted in the form of asymmetric $C_{p,mean}$ with respect to $\phi = 180^\circ$, may be partly responsible for this discrepancy. The asymmetry is likely to be due to a slight, imperceptible misalignment with the oncoming flow in the installation of the tandem-cylinder model in the wind tunnel. In the controlled case, the computed mean pressure coefficient is in good agreement with the experimental measurements. The computed r.m.s. of pressure fluctuations in the controlled case is also in general agreement with the experimental results except in the region close to the front stagnation point, where it is under-predicted. Overall, the numerical solutions predict well the effect of plasma flow control in terms of surface-pressure distributions.

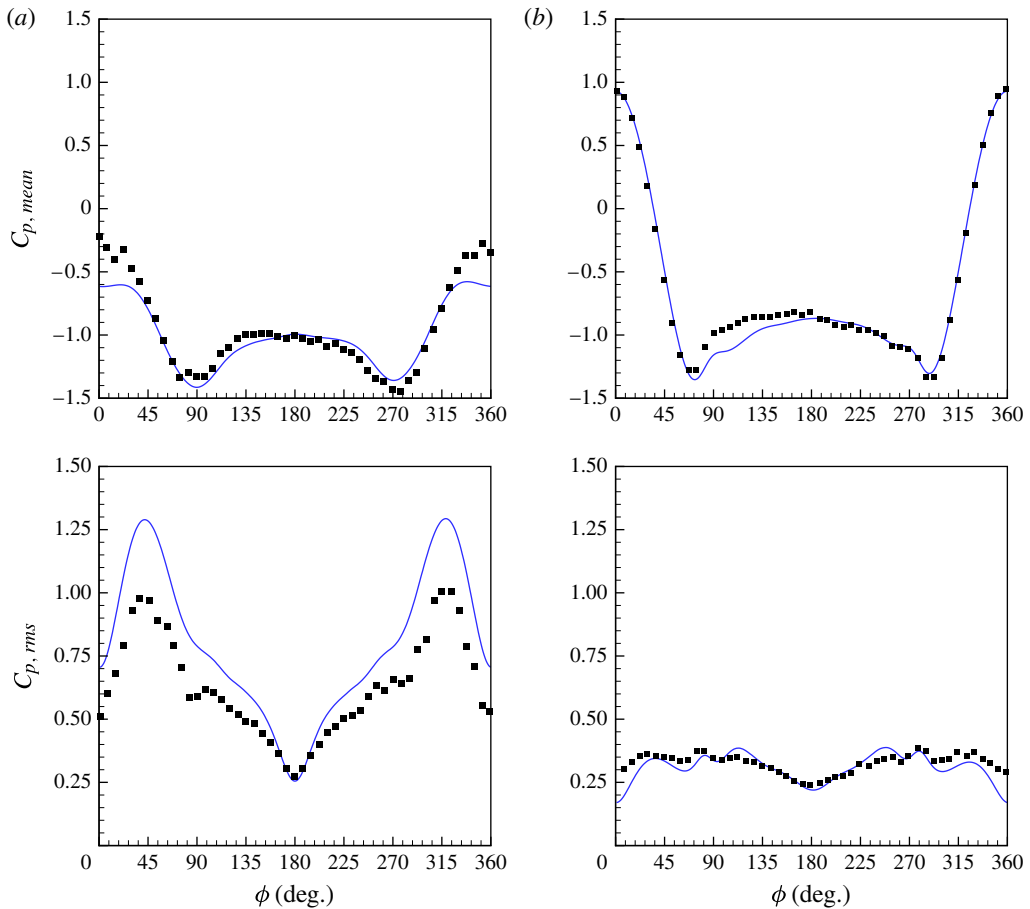


FIGURE 8. (Colour online) Pressure coefficient distribution over the downstream cylinder for (a) the baseline case and (b) the controlled case. —, LES; ■, experiment.

For both baseline and controlled cases, the power spectral density of pressure fluctuations on the surface of the downstream cylinder are shown in figure 9 at two different locations, $\phi = 45^\circ$ and $\phi = 105^\circ$. The pressure spectra are presented in dB with reference to 2×10^{-5} Pa, while the frequency is normalized by the free-stream velocity and the cylinder diameter. At these locations, the pressure spectra exhibit a strong shedding peak as well as broadband turbulence characteristics. In both cases, remarkably good agreement between LES and measurements is observed in terms of spectral peaks, peak frequencies, as well as the broadband spectral content over a wide range of frequencies. Without flow control, the major spectral peak is caused by the impingement of vortices shed from the upstream cylinder and occurs at the shedding frequency of $fD/U_\infty \approx 0.187$. When the plasma actuator is on, two major peaks with smaller magnitudes appear in the spectra. The first peak, at $fD/U_\infty \approx 0.2$, is associated with vortex shedding from the downstream cylinder, whereas the second peak, at $fD/U_\infty \approx 0.4$, is due to the vortex shedding from the upstream cylinder. Evidence of this will be shown below in the lift frequency spectra. The reduction in the peak unsteady pressure level caused by the flow control is approximately 11 dB

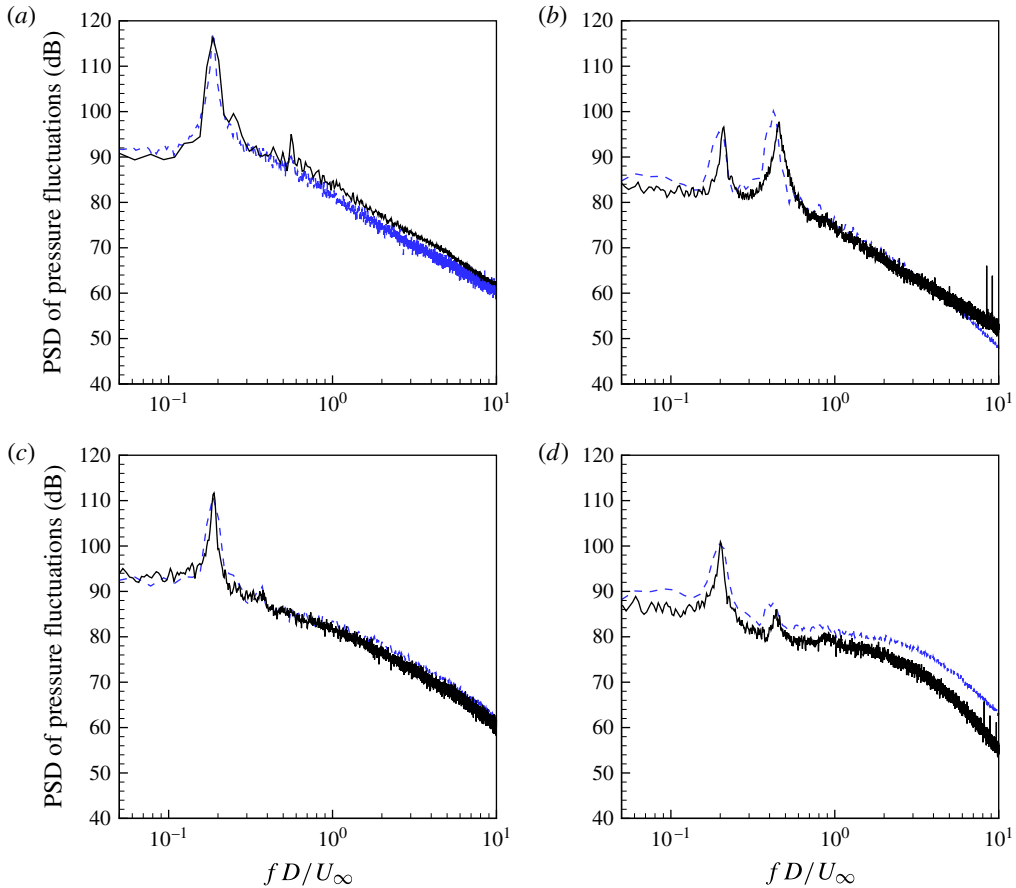


FIGURE 9. (Colour online) Power spectral density of pressure fluctuations at two locations on the surface of the downstream cylinder: (a,b) $\phi = 45^\circ$; (c,d) $\phi = 105^\circ$. (a,c) The baseline case; (b,d) the controlled case. —, Experiment; ---, LES.

at the first location ($\phi = 45^\circ$) and 12 dB at the second location ($\phi = 105^\circ$) compared to the baseline-case pressure level.

To explain the sources of the double spectral peaks in the surface-pressure spectra in the controlled case, the unsteady pressure lift and drag for both cylinders computed from LES are examined. Figure 10 shows the time history of lift and drag coefficients for the upstream cylinder. When the plasma actuation is applied at $tU_\infty/D = 164$, the mean drag coefficient is reduced by more than 60%. The lift and drag fluctuations are also reduced significantly. The frequency spectra of the unsteady lift and drag from LES are shown in figure 11 for both upstream and downstream cylinders. It is clear from the lift spectra that without flow control, the upstream and downstream cylinders share a common shedding peak and harmonics, which are caused by the vortex shedding from the upstream cylinder. When the plasma actuator is on, the upstream cylinder shows a single lift spectral peak at a much reduced magnitude and higher frequency, indicating weakened vortex shedding at a higher frequency. The lift spectrum for the downstream cylinder exhibits a peak at the frequency produced by the impingement of the vortices shed from the upstream cylinder. In addition, it shows a stronger peak at a lower frequency not shared by the upstream cylinder.

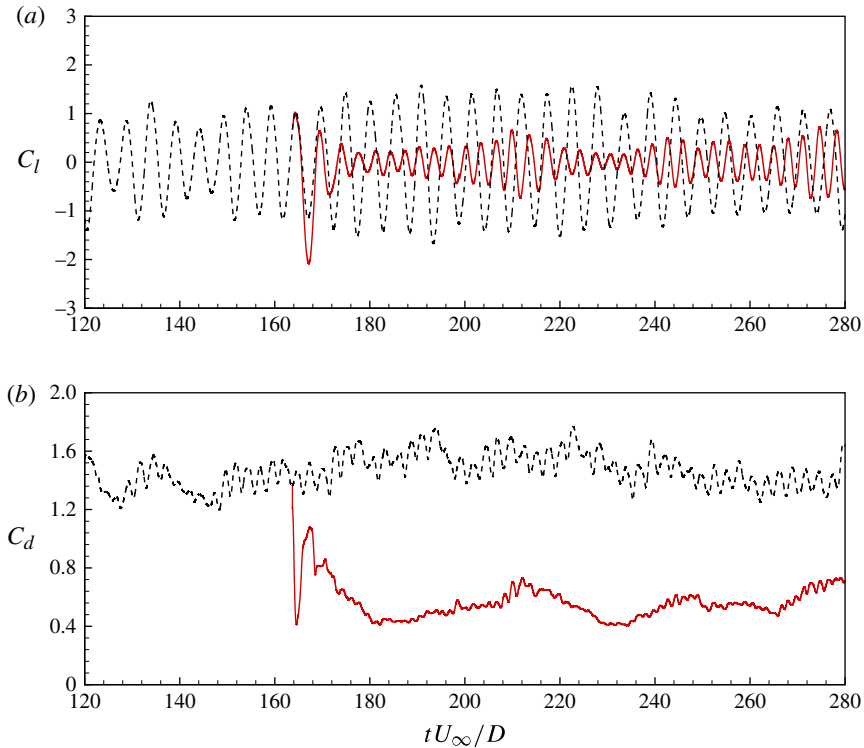


FIGURE 10. (Colour online) Time history of lift and drag coefficients for the upstream cylinder with and without plasma control: ----, plasma off; —, plasma on.

Evidently, this peak is produced by the vortex shedding from the downstream cylinder itself. The unsteady drag spectra support the above assessment and further confirm the reduction in shedding strength by flow control. Consequently, the noise produced by both cylinders is reduced since it is largely produced by the lift and drag dipoles. A detailed acoustic analysis is presented in the following section.

5. Acoustic analysis

A comparison of sound pressure spectra for the baseline and controlled cases is shown in figure 12. These spectra are plotted at four observer locations in the mid-span plane at $r = 1000D$ and $\theta = 45^\circ, 90^\circ, 135^\circ$, and 180° , where r originates from the mid-point between the two cylinders along the x -axis and θ is measured counter-clockwise from the streamwise direction (see figure 1). The acoustic pressure is normalized by the free-stream pressure P_∞ . The free-stream Mach number is $M = 0.2$, which is a typical value for a large passenger aircraft on landing approach. A dramatic reduction in the peak sound pressure level is observed at all observer locations as a result of the suppression of vortex shedding from the upstream cylinder. This is consistent with the drop in the lift and drag spectral levels shown in figure 11. When the cylinder diameter is much smaller than the acoustic wavelength, which is the case at the peak frequency and its first harmonic in the uncontrolled case, the acoustic source strength is directly proportional to the time derivative of the lift and drag (Curle 1955) and therefore a drop in lift and drag fluctuation levels causes a

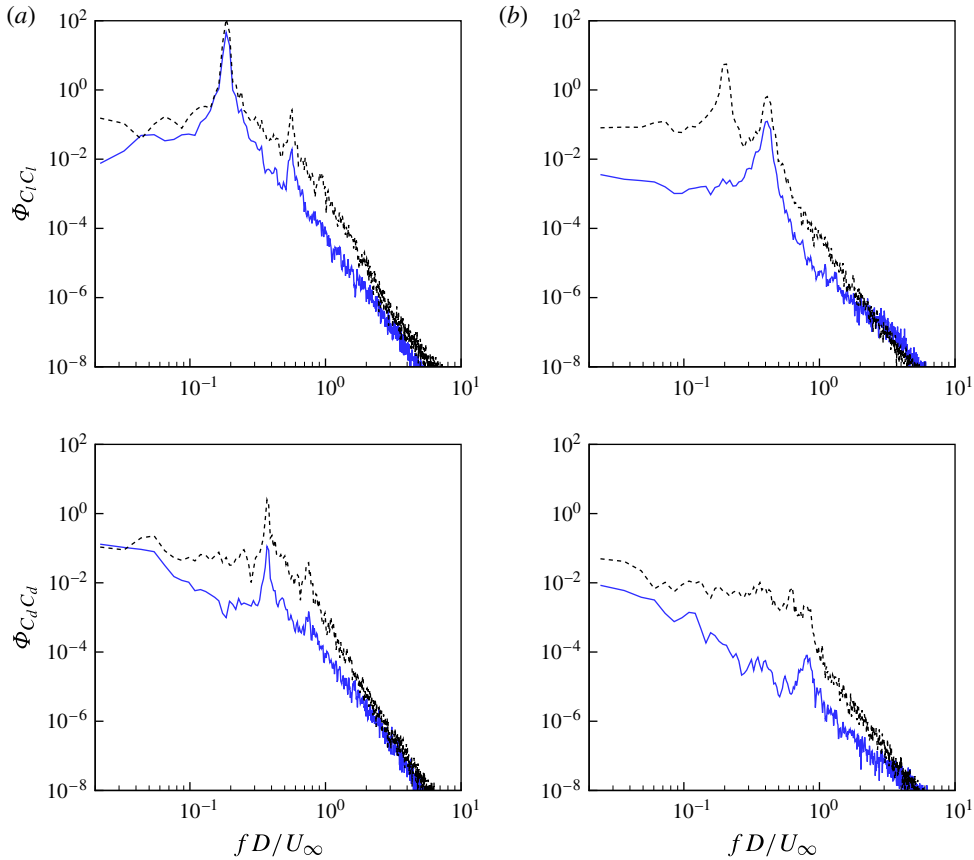


FIGURE 11. (Colour online) Power spectral density of pressure lift and drag coefficients for (a) the baseline case and (b) the controlled case. —, Upstream cylinder; ----, downstream cylinder.

noise reduction. It is noted from figure 12 that the broadband content of the sound spectra is reduced by the flow control as well. However, the higher-frequency spectral peak in the controlled case produced by vortex shedding from the downstream cylinder exceeds the spectral level for the baseline case at some observer locations (e.g. $\theta = 90^\circ$). Overall, the peak sound pressure level is reduced by at least 16 dB at all locations by flow control. The reduction is particularly significant in the upstream direction (figure 12d).

To examine contributions of different source regions to sound generation, the spanwise-averaged magnitudes of the three Lighthill stress components \tilde{T}_{11} , \tilde{T}_{12} and \tilde{T}_{22} at the vortex-shedding frequencies for the baseline and controlled cases are shown in figures 13–15 respectively. All three figures demonstrate the same source processes. For the baseline case at the shedding frequency of the upstream cylinder ($fD/U_\infty = 0.187$), the source terms are primarily concentrated behind the upstream cylinder. There are also two small regions of strong sources in front of the downstream cylinder due to the impingement of vortices from upstream. For the controlled case at $fD/U_\infty = 0.2$, which is the shedding frequency of the downstream cylinder, the source terms are concentrated solely in the near wake of the downstream cylinder. Finally, for

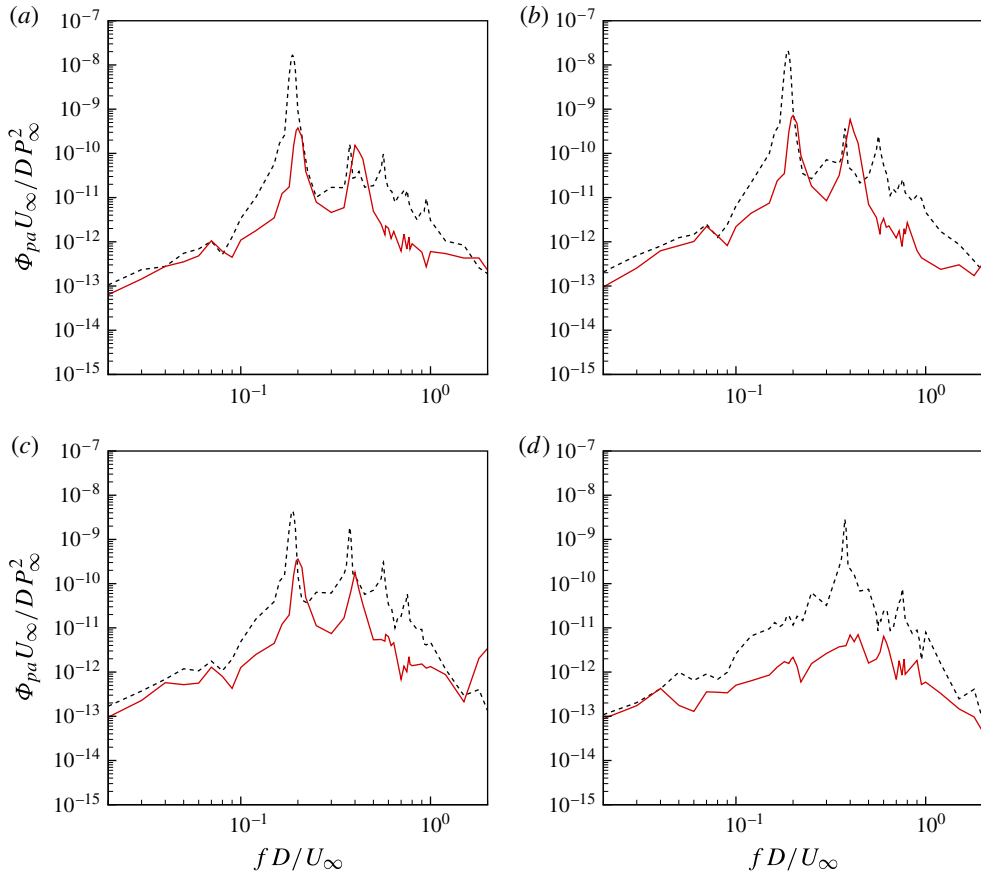


FIGURE 12. (Colour online) Sound pressure spectra for the baseline and controlled cases as a function of frequency at $r = 1000D$. (a) $\theta = 45^\circ$; (b) $\theta = 90^\circ$; (c) $\theta = 135^\circ$; (d) $\theta = 180^\circ$. ----, plasma off; —, plasma on.

the controlled case at $f D / U_\infty = 0.4$, which is the shedding frequency of the upstream cylinder, the source distributions are qualitatively similar to the uncontrolled case at the shedding frequency; the sources are strongest in the near wake of the upstream cylinder due to its vortex shedding and in front of the downstream cylinder due to the impingement. In terms of source strength, \tilde{T}_{11} and \tilde{T}_{12} are comparable and larger than \tilde{T}_{22} . It should also be noted that the relative importance of the source region depends not only on the source strength, but also its distance from the solid surface; sources closer to the cylinders are acoustically more efficient due to diffraction by the cylinder surface.

The use of the boundary-element method allows contributions from different source regions to the total sound to be separated. This is achieved by smoothly damping the Lighthill stress away from the region of interest and performing calculations based on the remaining sources. This method of source isolation is not exact but provides a convenient and effective means of analysis. In the present work, the damping starts half-way between the two cylinders ($x/D = 2$) and either extends downstream to isolate sources induced by the upstream cylinder or extends upstream

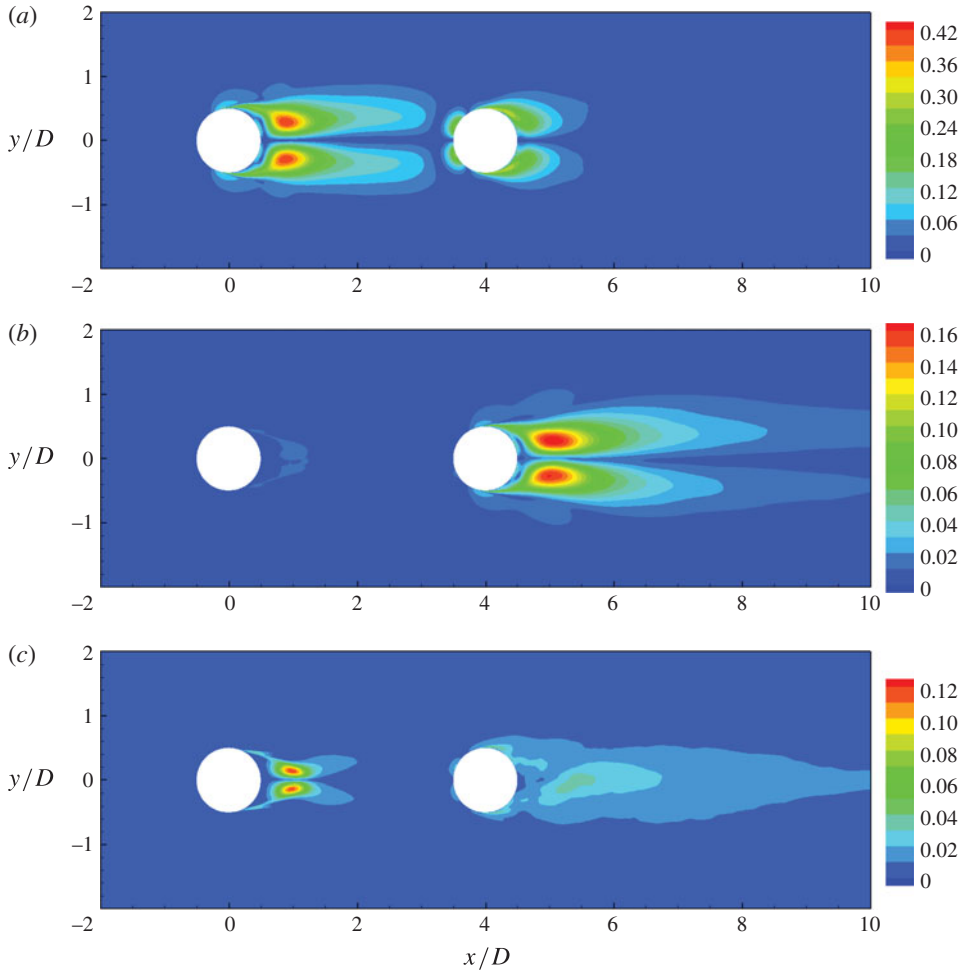


FIGURE 13. Contours of Lighthill's stress component $|\tilde{T}_{11}|/\rho_{\infty}U_{\infty}^2$: (a) plasma off, $fD/U_{\infty} = 0.187$; (b) plasma on, $fD/U_{\infty} = 0.2$; (c) plasma on, $fD/U_{\infty} = 0.4$.

to isolate sources induced by the downstream cylinder. Additional damping is applied starting at $x/D = 12$ and extending to the exit of the computational domain to prevent spurious sound due to a sudden truncation of the source terms at the exit (Wang, Lele & Moin 1996).

Figure 16 shows the predicted acoustic power spectra from sources around the two cylinders separately and the total sound power spectra at two far-field locations $r = 1000D$, $\theta = 90^\circ$ and 180° . The spectra at other angles away from upstream and downstream directions are qualitatively similar to that at $\theta = 90^\circ$. For the baseline case, both cylinders contribute nearly equally to the total sound over all frequencies. The downstream cylinder contributes slightly more than the upstream one, highlighting vortex impingement as an important source mechanism along with vortex shedding. The role of turbulence impingement as an acoustic source is well known in generating airfoil leading-edge noise as in the rod-airfoil benchmark problem (e.g. Jacob *et al.* 2005; Eltaweel & Wang 2011; Giret *et al.* 2014). It is also discussed extensively by Yang & Wang (2009, 2013) in the context of noise induced by roughness elements

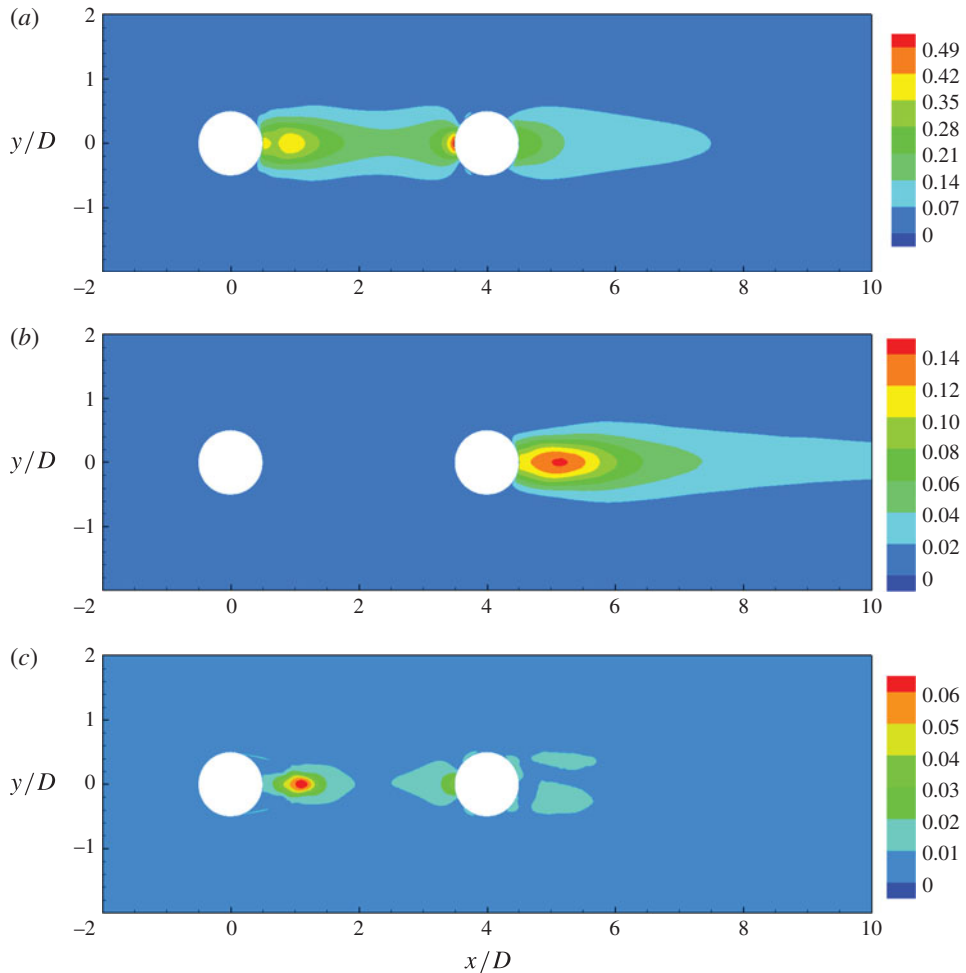


FIGURE 14. Contours of Lighthill's stress component $|\tilde{T}_{12}|/\rho_{\infty}U_{\infty}^2$: (a) plasma off, $fD/U_{\infty} = 0.187$; (b) plasma on, $fD/U_{\infty} = 0.2$; (c) plasma on, $fD/U_{\infty} = 0.4$.

in a turbulence boundary layer. For the controlled case, the downstream cylinder dominates sound generation at most frequencies including its own shedding frequency (the primary spectral peak). The only exception is at the shedding frequency of the upstream cylinder (the second spectral peak), where the upstream cylinder makes a larger contribution at θ angles away from the upstream and downstream directions.

The results presented in figures 12 and 16 confirm that the use of plasma actuators on the upstream cylinder is an effective strategy for noise reduction, since it suppressed the largest noise source caused by the upstream cylinder vortex shedding. Further reduction in noise requires reducing both spectral peaks associated with vortex shedding from both cylinders. Since these two peaks are of similar magnitude, adding plasma actuators on the downstream cylinder will not be sufficient. Rather, this should be considered in conjunction with further optimization of the actuators on the upstream cylinder with the goal of achieving overall airframe noise reduction.

Figures 17 and 18 show the directivities of sound for the baseline and controlled cases, respectively, at four different frequencies. Only one-half of the space is shown

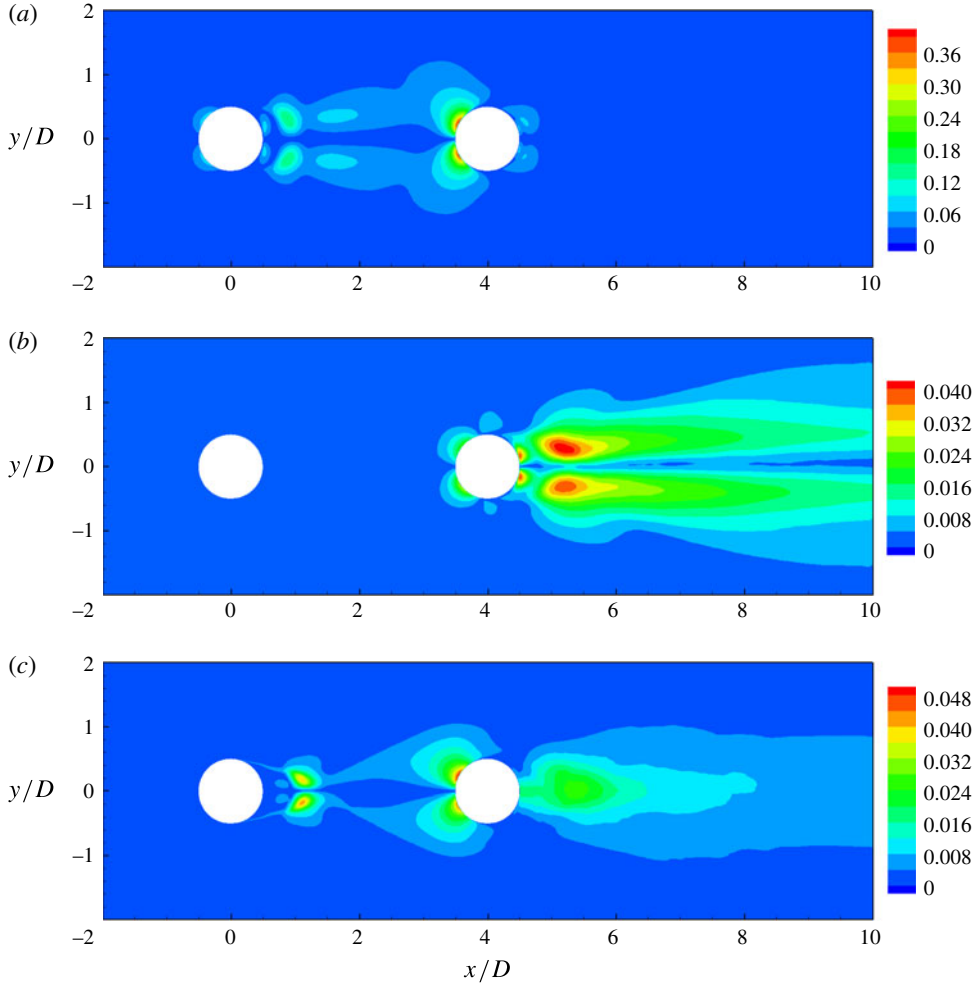


FIGURE 15. Contours of Lighthill's stress component $|\tilde{T}_{22}|/\rho_{\infty}U_{\infty}^2$: (a) plasma off, $fD/U_{\infty} = 0.187$; (b) plasma on, $fD/U_{\infty} = 0.2$; (c) plasma on, $fD/U_{\infty} = 0.4$.

due to symmetry. In each case, contributions from the upstream and downstream cylinders are plotted along with the total sound. In the baseline case, the directivities show a dominance of the lift dipoles, modified by flow convection and interference between sound signals generated or reflected from the two cylinders, at the main shedding frequency $fD/U_{\infty} = 0.187$ and its second harmonic $fD/U_{\infty} = 0.56$ (see figure 17a,c). Although the shedding is produced by the upstream cylinder, the sound generated by the downstream cylinder at these frequencies is stronger than that by the upstream cylinder, again indicating the pre-eminent role of wake impingement on the downstream cylinder as a noise source. As shown in figures 13–15, the interaction of the wake with the downstream cylinder produces strong sound sources adjacent to the front surface of the downstream cylinder. The close proximity between the source and the cylinder promotes efficient conversion of flow energy to acoustic energy through diffraction. At $fD/U_{\infty} = 0.375$ and 0.754 , which are the second and fourth harmonics of the upstream-cylinder shedding frequency, the

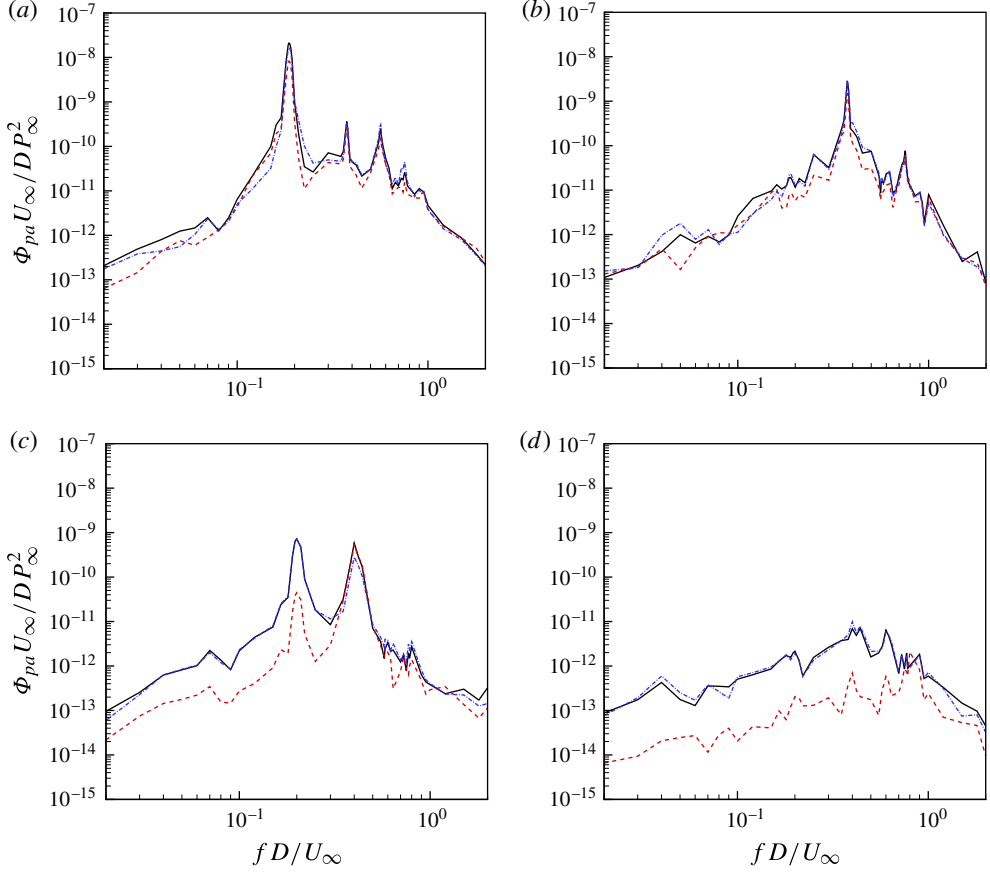


FIGURE 16. (Colour online) Sound pressure spectra for (a,b) the baseline and (c,d) the controlled cases as a function of frequency at $r = 1000D$ and (a,c) $\theta = 90^\circ$ and (b,d) 180° . —, Total sound; ---, sound from first cylinder; -·-, sound from second cylinder.

directivities show dominance by drag dipoles modified by convection and interference (see figure 17b,d). The contribution from the downstream cylinder due to wake impingement is again larger than the contribution from the upstream cylinder due to vortex shedding.

In the controlled case, shown in figure 18, the sound directivities at the shedding frequencies of the downstream cylinder ($fD/U_\infty = 0.2$) and the upstream cylinder ($fD/U_\infty = 0.4$) both show a dominance of the modified lift dipoles (see figure 18a,b). The upstream cylinder contributes very little at the downstream-cylinder shedding frequency, whereas the downstream cylinder contributes significantly at the upstream-cylinder shedding frequency due to wake impingement. At higher harmonics of the shedding frequencies, $fD/U_\infty = 0.6$ and 0.8 (see figure 18c,d), the total directivities are dominated by the downstream cylinder. They exhibit combinations of lift- and drag-dipole sound, and interference between sound signals from both cylinders becomes more significant as frequency increases. The overall sound pressure levels are reduced significantly by flow control at all frequencies.

Figures 19 and 20 illustrate the relative contributions of the direct quadrupole radiation (volume integral in (3.2)) and the scattered sound (surface integral in (3.2))

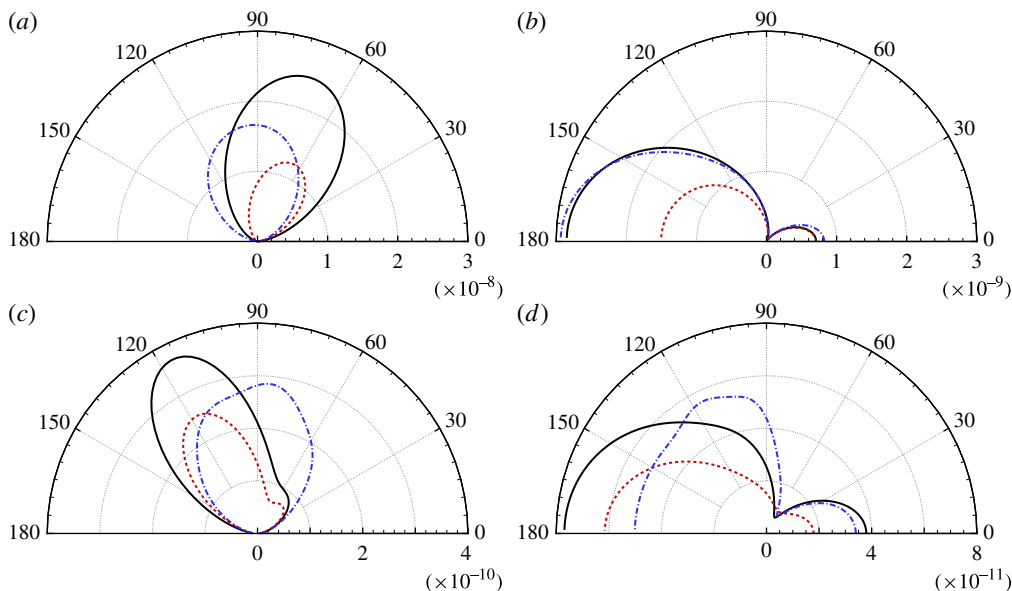


FIGURE 17. (Colour online) Directivity of baseline sound pressure spectra $\Phi_{pa}U_{\infty}/P_{\infty}^2D$ at $r = 1000D$ and four frequencies: (a) $fD/U_{\infty} = 0.187$; (b) $fD/U_{\infty} = 0.375$; (c) $fD/U_{\infty} = 0.56$; (d) $fD/U_{\infty} = 0.754$. —, Total sound; ----, sound from first cylinder; ···, sound from second cylinder.

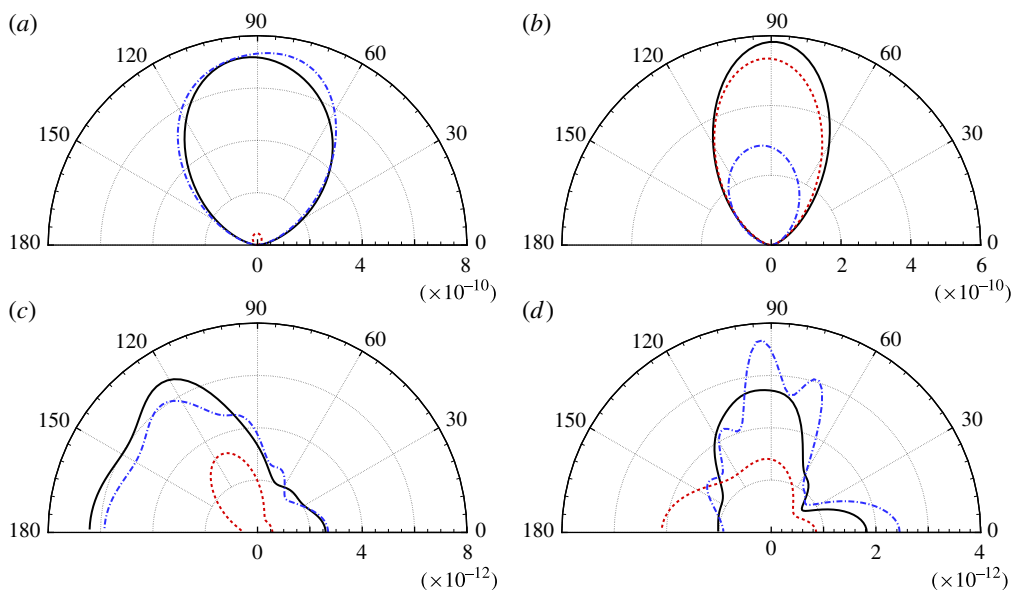


FIGURE 18. (Colour online) Directivity of controlled sound pressure spectra $\Phi_{pa}U_{\infty}/P_{\infty}^2D$ at $r = 1000D$ and four frequencies: (a) $fD/U_{\infty} = 0.2$; (b) $fD/U_{\infty} = 0.4$; (c) $fD/U_{\infty} = 0.6$; (d) $fD/U_{\infty} = 0.8$. —, Total sound; ----, sound from first cylinder; ···, sound from second cylinder.

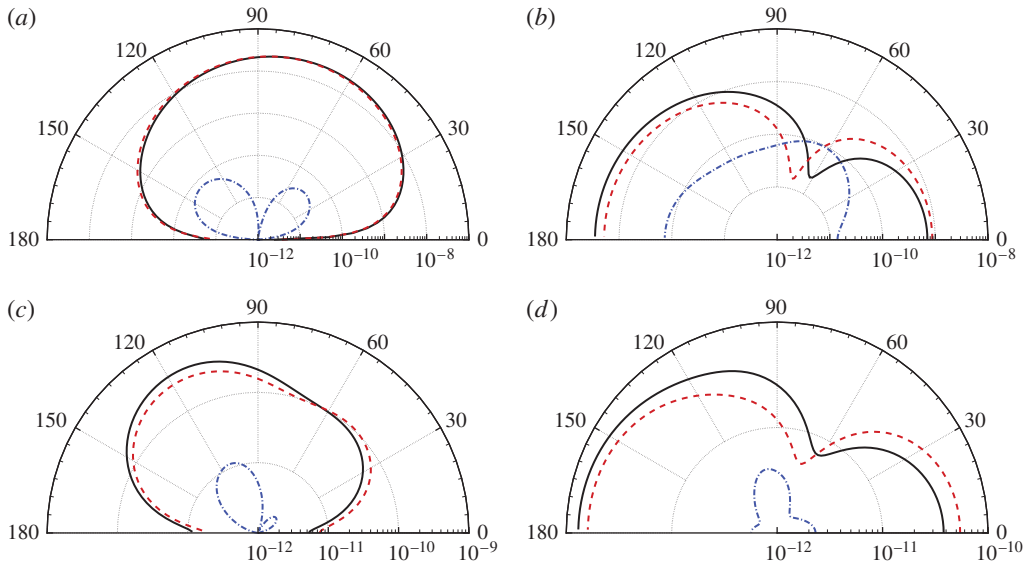


FIGURE 19. (Colour online) Contributions of direct quadrupole sound and scattered sound to the total sound pressure spectra $\Phi_{pa}U_\infty/P_\infty^2 D$ for the baseline case. The directivity of the spectra is plotted at $r = 1000D$ and four frequencies: (a) $fD/U_\infty = 0.187$; (b) $fD/U_\infty = 0.375$; (c) $fD/U_\infty = 0.56$; (d) $fD/U_\infty = 0.754$. —, Total sound; ----, scattered sound; - · -, direct sound.

for the baseline and controlled cases, respectively. In each case, the pressure spectra of the quadrupole sound and scattered sound are plotted along with the total sound pressure spectra at $r = 1000D$ and four frequencies. The quadrupole sound is very weak overall compared to the scattered sound (note the logarithmic scale used in the figures), as expected for a low-Mach-number flow, but the difference decreases with increasing frequency as the cylinders become acoustically less compact. The relative strengths of the quadrupole and scattered sound are highly dependent on the frequency and direction. At certain frequencies and observer angles, the quadrupole sound can reach levels comparable to or even higher than the scattered sound (see, for example, figure 19*b* near $\theta = 70^\circ$).

Finally, it should be pointed out that the acoustic results presented in this section are based on the convected Lighthill equation and therefore subject to limitations of that equation. While the predictions are valid for most observer angles in figures 17–20, their accuracy is compromised at shallow angles (say, $-30^\circ < \theta < 30^\circ$) because the Lighthill equation does not take into account the effect of non-uniform and turbulent flows on sound propagation. These effects become significant at shallow angles and high frequencies, as the propagation distance inside the turbulent wake becomes comparable to or longer than the acoustic wavelength.

6. Conclusion

In this study, the effectiveness of SDBD plasma actuators for suppressing surface-pressure fluctuations, and consequently flow-induced noise, is demonstrated experimentally and numerically in a tandem-cylinder configuration at Reynolds number of 22 000. At a free-stream Mach number of 0.2, the peak fluctuating pressure levels at the two measurement locations on the downstream cylinder, $\phi = 45^\circ$ and

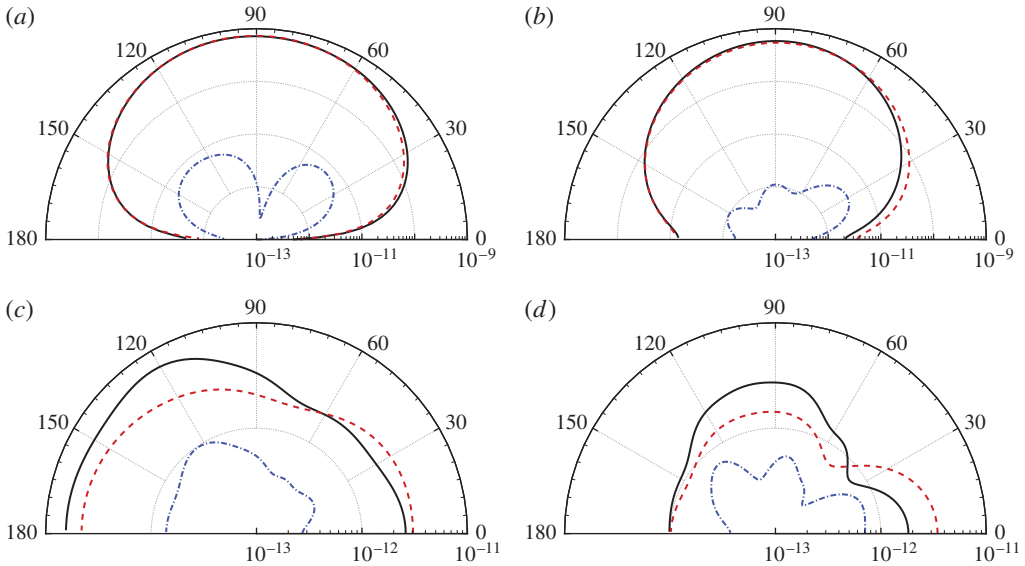


FIGURE 20. (Colour online) Contributions of direct quadrupole sound and scattered sound to the total sound pressure spectra $\Phi_{pa} U_\infty / P_\infty^2 D$ for the controlled case. The directivity of the spectra is plotted at $r = 1000D$ and four frequencies: (a) $fD/U_\infty = 0.2$; (b) $fD/U_\infty = 0.4$; (c) $fD/U_\infty = 0.6$; (d) $fD/U_\infty = 0.8$. —, Total sound; ---, scattered sound; -·-, direct sound.

105°, are reduced by 11 and 12 dB, respectively, compared to the uncontrolled baseline values. The peak sound pressure level is reduced by at least 16 dB.

The numerical approach employed in the present study is based on incompressible LES for the flow field, a semi-empirical plasma actuation model calibrated by experimentally measured mean velocity, and Lighthill's equation solved using a boundary-element method for the radiated acoustic field. For both baseline and controlled cases, numerical results show excellent agreement with experimental data in terms of wake profiles, turbulence intensity, and surface-pressure fluctuations on the downstream cylinder. In particular, they capture the frequency spectra of pressure fluctuations on the downstream cylinder with remarkable accuracy in terms of both the shedding peaks and broadband content over a wide range of frequencies. LES with the plasma model correctly accounts for the control effect in terms of shedding suppression, reduced wake turbulence, and greatly reduced surface-pressure fluctuations.

With a fully validated flow-field solution, the LES database is used to extend the experimental results to the acoustic field and perform a systematic analysis of the noise-source and noise-reduction mechanisms. The use of a boundary-element method allows noise from different source regions to be identified. It is shown that both vortex shedding and vortex impingement on the downstream cylinder are important source mechanisms. Noise reduction is achieved through suppression of vortex shedding from the upstream cylinder, which results in reduced intensity of turbulence impinging on the downstream cylinder. Without flow control, the flow and acoustic fields are dominated by the vortex shedding from the upstream cylinder, and the downstream cylinder does not produce independent vortex shedding. When flow control is applied on the upstream cylinder, separation from the upstream cylinder

is delayed, resulting in a narrower and more stable turbulent wake. Vortex shedding is much weaker and takes place farther downstream at a higher frequency. In the meantime, the downstream cylinder generates its independent vortex shedding because it is now in a more benign turbulent wake. The vortex shedding from both cylinders makes comparable contributions to the overall sound field. Further noise reduction is possible by improving the control efficiency on the upstream cylinder and applying plasma actuators on the downstream cylinder, so that vortex shedding from both cylinders can be further weakened or eliminated.

It is worth pointing out that although the present computational analysis is for $Re_D = 22\,000$, similar control effects on the flow field have been observed experimentally for subcritical Reynolds numbers up to $Re_D = 172\,000$. Based on the physical understanding of noise reduction mechanisms gained from this study, it is reasonable to expect similar levels of noise reduction in these high-Reynolds-number flows as well.

Acknowledgements

This work was supported by NASA through Cooperative Agreement NNX07AO09A. Computations were performed on the NASA Advanced Supercomputing facilities and University of Notre Dame Center for Research Computing facilities. A portion of this work in an earlier version was presented in *AIAA Paper* 2010-3790, 16th AIAA/CEAS Aeroacoustic Conference, Stockholm, Sweden, 7–9 June, 2010.

Appendix. Validation of acoustic solution method

To demonstrate the accuracy of the acoustic solution method described in §3.2, it is applied to two aeroacoustic problems for which previous experimental or numerical results are available for comparison.

The first validation case is the sound of flow over a circular cylinder at $Re_D = 10\,000$ and free-stream Mach number $M = 0.2$. The results are compared with those of Khalighi *et al.* (2010) computed directly from a compressible LES with a sixth-order compact finite-difference scheme as well as their solutions using a hybrid approach with a boundary-element method. The simulation method for the turbulent flow is the same as that for the tandem cylinders. The computational domain size is $100D \times 100D \times \pi D$ in the streamwise (x), cross-stream (y), and spanwise (z) directions, respectively. The mesh size is 1.44×10^7 cells with 64 cells in the spanwise direction. In the direct computation of Khalighi *et al.* (2010) conducted on a structured, O-type mesh, the mesh size is 8.85×10^6 cells with 48 cells covering the same spanwise length.

Figure 21 shows a comparison of the acoustic pressure spectra at two observer locations $(x, y) = (-1.2D, 16.2D)$ and $(-13.5D, 0)$, with $(0, 0)$ being the cylinder centre. To be consistent with the direct computation, the acoustic problem is treated as that of an infinite span with periodic extensions outside the computational domain. The present computations show good overall agreement with those of Khalighi *et al.* (2010) in terms of both spectral peaks and broadband contents. The levels at the shedding frequency and its first few harmonics are stronger in the present simulation, which is primarily attributed to better grid resolution by the unstructured mesh in the separated shear layers, leading to stronger vortex shedding. When the mesh of Khalighi *et al.* (2010) was used in the flow simulation, the difference in peak levels relative to the directly computed sound of Khalighi *et al.* (2010) was found to be reduced from 3.0 to 1.1 dB at the first location and from 4.4 to 1.2 dB at the second location. Other factors, including different numerical algorithms and statistical

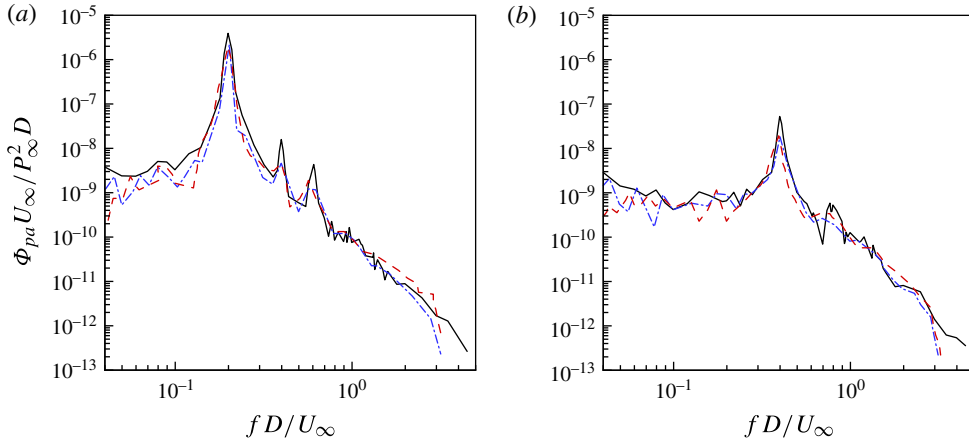


FIGURE 21. (Colour online) Sound pressure spectra for flow over a circular cylinder at $Re_D = 10\,000$ and $M = 0.2$, at (a) $(x, y) = (-1.2D, 16.2D)$ and (b) $(x, y) = (-13.5D, 0)$. —, Present computation; ----, direct computation of Khalighi *et al.* (2010); —·—, hybrid computation of Khalighi *et al.* (2010).

processing methods employed in the two studies, may have also contributed to the observed differences. Note that the direct computation of Khalighi *et al.* (2010) accounts for full flow–acoustic interactions including the effect of the non-uniform and turbulent flow on sound propagation, whereas in the Lighthill solution only the convection effect of the uniform free stream is included. The overall good agreement between the two solutions confirms that, because of the low Mach number, the refraction and scattering effects of the turbulent wake on sound propagation are insignificant.

The second validation case is the benchmark aeroacoustic experiment involving flow over a rod–airfoil configuration performed by Jacob *et al.* (2005). As illustrated in figure 22, a NACA 0012 airfoil is placed one chord (C) downstream of a cylindrical rod of diameter $D = 0.1C$. The rod axis is parallel to the airfoil leading edge, and the spanwise extent of the rod and airfoil is $3C$ in the experiment. Among the various Reynolds numbers and Mach numbers examined in the experiment, the case with chord Reynolds number $Re_C = 480\,000$ and free-stream Mach number $M = 0.2$ is selected for computation because it has the most comprehensive experimental data. For brevity only the key comparisons with experimental results are presented here.

The flow simulation is again with the same incompressible LES code as for the tandem cylinders. In a computational domain of size $6C$ (streamwise, x) \times $6C$ (cross-stream, y) \times $0.1\pi C$ (spanwise, z), a total of 2.05×10^7 mesh cells with 96 cells in the spanwise direction are employed. The velocities are fixed at the uniform free-stream values $(U_\infty, 0, 0)$ at the inlet, top and bottom boundaries, and zero on the rod and airfoil surfaces. Periodic conditions are applied in the statistically homogeneous spanwise direction. In the acoustic calculation, the free-stream convection is neglected because the experiment was conducted in an open-jet facility with negligible velocities outside the jet. The refraction and scattering by jet shear layers are also neglected on the basis of low-Mach-number flow and not-too-low observer angles.

Figure 23 shows a comparison of the acoustic pressure spectra predicted by the numerical simulation and the experimental data of Jacob *et al.* (2005) at two

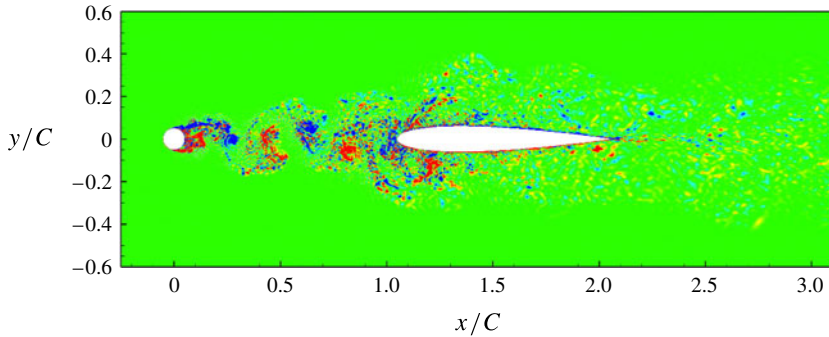


FIGURE 22. (Colour online) Flow over a rod–airfoil configuration in the experiment of Jacob *et al.* (2005), shown as contours of instantaneous spanwise vorticity $\omega_z C/U_\infty$ in a spanwise plane obtained from LES (contour levels from -30 to 30 with increment 6).

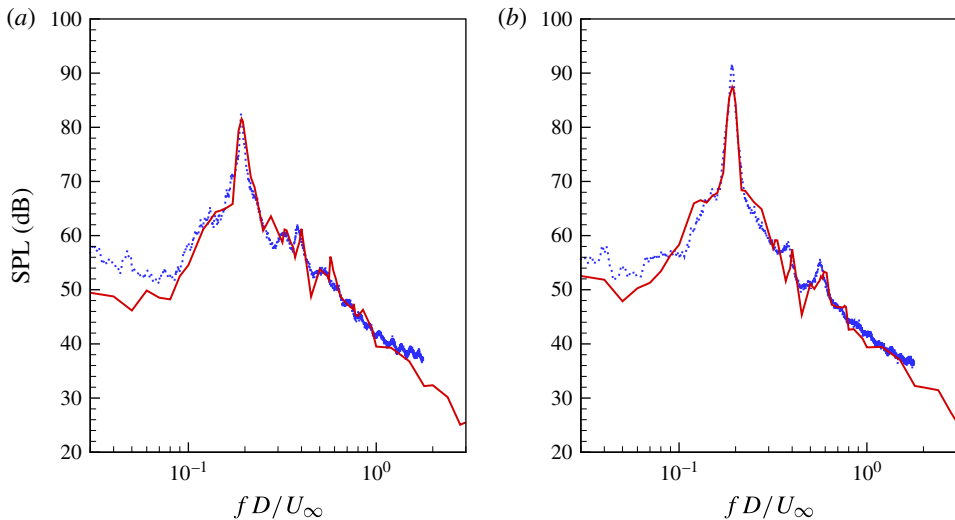


FIGURE 23. (Colour online) Acoustic pressure spectra (ref. 2×10^{-5} Pa) for flow over a rod–airfoil configuration in the mid-span plane at $r = 18.5C$ and two observer angles: (a) $\theta = 45^\circ$; (b) $\theta = 90^\circ$. —, Numerical solution; \cdots , experiment (Jacob *et al.* 2005).

locations in the mid-span plane: $r = 18.5C$ and $\theta = 45^\circ$ and 90° , where r originates from the airfoil centre and θ is counter-clockwise from the downstream direction. The numerical results capture correctly all the important spectral features, including the vortex-shedding peak, its harmonics and the broadband sound over a wide frequency range. The peak levels are under-predicted by 0.8 dB at $\theta = 45^\circ$ and 4.3 dB at $\theta = 90^\circ$. This may be partly due to an under-estimate of the spanwise coherence length at the shedding frequency, which was assumed to be no larger than the spanwise computational domain size L_z because the sound spectrum for the entire experimental span S was assumed to be S/L_z times the spectrum from the computational domain. If a spanwise coherence length of $7D$ estimated from the experiment (Jacob *et al.* 2005) is used to scale the sound pressure spectra from the limited-span simulation to the full-span experiment, the spectral peaks are increased by 3.5 dB, resulting in a 2.7 dB over-prediction at $\theta = 45^\circ$ and 0.8 dB under-prediction at $\theta = 90^\circ$.

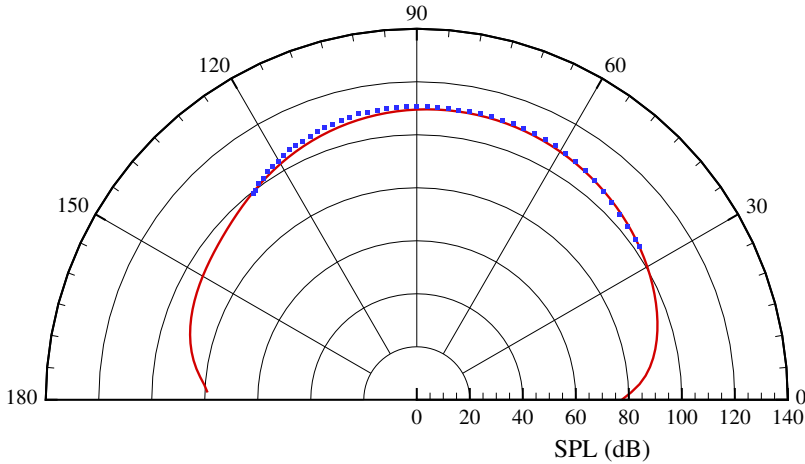


FIGURE 24. (Colour online) Directivity of acoustic power (ref. 2×10^{-5} Pa) in the mid-span plane at $r = 18.5C$ for flow over a rod–airfoil configuration. —, Numerical solution; ■, experiment (Jacob *et al.* 2005).

The discrepancies at the low-frequency end are at least partially caused by facility noise in the experiment. As shown in figure 11 of Jacob *et al.* (2005), the measured sound pressure spectrum at $\theta = 90^\circ$ is dominated by background noise for $fD/U_\infty \leq 0.05$.

In figure 24, the computed acoustic directivity is compared with the measured values in terms of the acoustic power (integration of the spectrum over all frequencies) at $r = 18.5C$. Very good overall agreement is observed with a maximum discrepancy of 2.2 dB at $\theta = 102^\circ$. The discrepancies at $\theta = 45^\circ$ and 90° are 0.5 dB and 1.1 dB, respectively. The numerical results extend to shallow angles in both upstream and downstream directions, but those in the downstream direction are inaccurate because the large propagation distance inside the turbulent wake can cause significant refraction and scattering of the sound, which are not included in the Lighthill equation.

The above two examples establish the validity and accuracy of the computational method employed in the present study for the sound of flow over tandem cylinders. In particular, the rod–airfoil case contains all the elements of tandem-cylinder aeroacoustics, including the sound generation by vortex shedding and wake interaction with the downstream object, as well as the acoustic interactions with both objects and the turbulent flow. In fact, the rod–airfoil case is computationally more demanding because of the higher airfoil chord Reynolds number and the trailing-edge self-noise (Wang & Moin 2000). The accurate acoustic predictions by the current approach provide confidence in the tandem-cylinder acoustic predictions and analysis presented in this paper.

REFERENCES

- ARIE, M., KIYA, M., MORIYA, M. & MORI, H. 1983 Pressure fluctuations on the surface of two circular cylinders in tandem arrangement. *Trans. ASME: J. Fluids Engng* **105**, 161–167.
- BRÉS, G. A., FREED, D., WESSELS, M., NOELTING, S. & PÉROT, F. 2012 Flow and noise predictions for the tandem cylinder aeroacoustic benchmark. *Phys. Fluids* **24**, 036101.

- CORKE, T. C., ENLOE, C. L. & WILKINSON, S. P. 2010 Dielectric barrier discharge plasma actuators for flow control. *Annu. Rev. Fluid Mech.* **42**, 505–529.
- CURLE, N. 1955 The influence of solid boundaries upon aerodynamic sound. *Proc. R. Soc. Lond. A* **231**, 505–514.
- DOOLAN, C. J. 2009 Flow and noise simulation of the NASA tandem cylinder experiment using OpenFOAM. *AIAA Paper* 2009-3157.
- ELTAWHEEL, A. & WANG, M. 2011 Numerical simulation of broadband noise from airfoil–wake interaction. *AIAA Paper* 2011-2802.
- GIRET, J.-C., SENGISSEN, A., MOREAU, S., SANJOSÉ, M. & JOUHAUD, J.-C. 2014 Noise prediction and analysis of a rod–airfoil configuration using unstructured LES. *AIAA J.* (in press).
- HAO, J., ELTAWHEEL, A. & WANG, M. 2013a Sound generated by boundary-layer flow over small steps: effect of step non-compactness. *AIAA J.* **51**, 1770–1775.
- HAO, J., WANG, M., JI, M. & WANG, K. 2013b Flow noise induced by small gaps in low-Mach-number turbulent boundary layers. *Phys. Fluids* **25**, 110821.
- IGARISHI, T. 1981 Characteristics of the flow around two circular cylinders in tandem, 1st report. *Bull. JSME* **B24**, 232–331.
- IGARISHI, T. 1984 Characteristics of the flow around two circular cylinders in tandem, 2nd report. *Bull. JSME* **B27**, 2380–2387.
- JACOB, M. C., BOUDET, J., CASALINO, D. & MICHARD, M. 2005 A rod–airfoil experiment as benchmark for broadband noise modeling. *Theor. Comput. Fluid Dyn.* **19**, 171–196.
- JENKINS, L. N., KHORRAMI, M. R., CHOUDHARI, M. M. & MCGINLEY, C. B. 2005 Characterization of unsteady flow structures around tandem cylinders for component interaction studies in airframe noise. *AIAA Paper* 2005-2812.
- JENKINS, L. N., NEUHART, D. H., MCGINLEY, C. B., CHOUDHARI, M. M. & KHORRAMI, M. R. 2006 Measurement of unsteady wake interference between tandem cylinders. *AIAA Paper* 2006-3202.
- JESTER, W. & KALLINDERIS, T. 2003 Numerical study of incompressible flow about fixed cylinder pairs. *J. Fluids Struct.* **17**, 561–577.
- KHALIGHI, Y., MANI, A., HAM, F. & MOIN, P. 2010 Prediction of sound generated by complex flows at low Mach numbers. *AIAA J.* **48**, 306–316.
- KHORRAMI, M. R., CHOUDHARI, M. M., JENKINS, L. N. & MCGINLEY, C. B. 2007 Unsteady flowfield around tandem cylinders as prototype for component interaction in airframe noise. *AIAA J.* **45**, 1930–1941.
- KIM, D. & WANG, M. 2009 Large-eddy simulation of flow over a circular cylinder with plasma-based control. *AIAA Paper* 2009-1080.
- KOZLOV, A. V. & THOMAS, F. O. 2011a Bluff-body flow control via two types of dielectric barrier discharge plasma actuation. *AIAA J.* **49**, 1919–1931.
- KOZLOV, A. V. & THOMAS, F. O. 2011b Plasma flow control of cylinders in a tandem configuration. *AIAA J.* **49**, 2183–2193.
- LIGHTHILL, J. M. 1952 On sound generated aerodynamically. Part I. General theory. *Proc. R. Soc. Lond. A* **211**, 564–587.
- LIN, J.-C., YANG, Y. & ROCKWELL, D. 2002 Flow past two cylinders in tandem: instantaneous and averaged flow structure. *J. Fluids Struct.* **16**, 1059–1071.
- LJUNGKRONA, L., NORBERG, C. & SUNDEN, B. 1991 Free-stream turbulence and tube spacing effects on surface pressure fluctuations for two tubes in an in-line arrangement. *J. Fluids Struct.* **5**, 701–727.
- LOCKARD, D. P., CHOUDHARI, M. M., KHORRAMI, M. R., NEUHART, D. H., HUTCHESON, F. V., BROOKS, T. F. & STEAD, D. J. 2008 Aeroacoustic simulations of tandem cylinders with subcritical spacing. *AIAA Paper* 2008-2862.
- LOCKARD, D. P., KHORRAMI, M. R., CHOUDHARI, M. M., HUTCHESON, F. V., BROOKS, T. F. & STEAD, D. J. 2007 Tandem cylinder noise predictions. *AIAA Paper* 2007-3450.
- MAHESH, K., CONTANTINESCU, G. & MOIN, P. 1998 A numerical method for large-eddy simulation in complex geometries. *J. Comput. Phys.* **140**, 233–258.

- MITTAL, S., KUMAR, V. & RAGHUVANSHI, A. 1997 Unsteady incompressible flows past two cylinders in tandem and staggered arrangements. *Intl J. Numer. Meth. Fluids* **25**, 1315–1344.
- NEUHART, D. H., JENKINS, L. N., CHOUDHARI, M. M. & KHORRAMI, M. R. 2009 Measurements of the flowfield interaction between tandem cylinders. *AIAA Paper* 2009-3275.
- OBERAI, A. A., ROKNALDIN, F. & HUGHES, T. J. R. 2002 Computation of trailing-edge noise due to turbulent flow over an airfoil. *AIAA J.* **40**, 2206–2216.
- SUZEN, Y. B., HUANG, P. G., JACOB, J. D. & ASHIPIS, D. E. 2005 Numerical simulation of plasma based flow control applications. *AIAA Paper* 2005-4633.
- THOMAS, F. O., CORKE, T. C., IQBAL, M., KOZLOV, A. V. & SCHATZMAN, D. 2009 Optimization of dielectric barrier discharge plasma actuators for active aerodynamic flow control. *AIAA J.* **47**, 2169–2178.
- THOMAS, F. O., KOZLOV, A. V. & CORKE, T. C. 2008 Plasma actuators for cylinder flow control and noise reduction. *AIAA J.* **46**, 1921–1931.
- WANG, M., FREUND, J. B. & LELE, S. K. 2006 Computational prediction of flow-generated sound. *Annu. Rev. Fluid Mech.* **38**, 483–512.
- WANG, M., LELE, S. K. & MOIN, P. 1996 Computation of quadrupole noise using acoustic analogy. *AIAA J.* **34**, 2247–2254.
- WANG, M. & MOIN, P. 2000 Computation of trailing-edge flow and noise using large-eddy simulation. *AIAA J.* **38**, 2201–2209.
- WEINMANN, M., SANDBERG, R. D. & DOOLAN, C. J. 2010 Flow and noise predictions for a tandem cylinder configuration using novel hybrid RANS/LES approaches. *AIAA Paper* 2010-3787.
- XU, G. & ZHOU, Y. 2004 Strouhal numbers in the wake of two inline cylinders. *Exp. Fluids* **37**, 248–256.
- YANG, Q. & WANG, M. 2009 Computational study of roughness-induced boundary-layer noise. *AIAA J.* **47**, 2417–2429.
- YANG, Q. & WANG, M. 2013 Boundary-layer noise induced by arrays of roughness elements. *J. Fluid Mech.* **727**, 282–317.
- ZDRAVKOVICH, M. M. 1985 Flow induced oscillations of two interfering circular cylinders. *J. Sound Vib.* **101**, 511–521.